Journal Pre-proof

Combining traditional and quantitative multiscale structural analysis to reconstruct the tectono-metamorphic evolution of migmatitic basements: The case of the Valpelline Series, Dent-Blanche Tectonic System, Western Alps

F. Caso, C.B. Piloni, M. Filippi, A. Pezzotta, E. Fazio, R. Visalli, G. Ortolano, M. Roda, M. Zucali

Please cite this article as: Caso, F., Piloni, C.B., Filippi, M., Pezzotta, A., Fazio, E., Visalli, R., Ortolano, G., Roda, M., Zucali, M., Combining traditional and quantitative multiscale structural analysis to reconstruct the tectono-metamorphic evolution of migmatitic basements: The case of the Valpelline Series, Dent-Blanche Tectonic System, Western Alps, *Journal of Structural Geology* (2024), doi: https://doi.org/10.1016/j.jsg.2024.105099.

This is a PDF file of an article that has undergone enhancements after acceptance, such as the addition of a cover page and metadata, and formatting for readability, but it is not yet the definitive version of record. This version will undergo additional copyediting, typesetting and review before it is published in its final form, but we are providing this version to give early visibility of the article. Please note that, during the production process, errors may be discovered which could affect the content, and all legal disclaimers that apply to the journal pertain.

1 **Combining traditional and quantitative multiscale structural analysis to reconstruct the**

2 **tectono-metamorphic evolution of migmatitic basements: the case of the Valpelline Series,**

3 **Dent-Blanche Tectonic System, Western Alps**

4 Caso F.[a*], Piloni C.B.[a], Filippi M.[a], Pezzotta A.[a], Fazio E.[b], Visalli R.[b], Ortolano G.[b], Roda M.[a],

5 Zucali M.[a]

6 [a]Department of Earth Sciences "A. Desio", University of Milan, Via Mangiagalli 34, 20133 Milan, Italy

7 [b]Department of Biological, Geological and Environmental Sciences, University of Catania, Catania, Italy

8 *corresponding author: fabiola.caso@unimi.it

9 Keywords: 3D outcrop models; quantitative multiscale structural analysis; X-ray maps; high-temperature deformation;

10 migmatites

Abstract

12 Due to the ongoing development of new technologies, many instruments are available to assist

13 geological investigations at different scales. These techniques, including 3D outcrop modelling from

14 aerial photogrammetry, and quantitative microstructural analysis are useful in crystalline basement

15 studies. This contribution combines traditional and quantitative multiscale structural analysis

16 techniques to the migmatitic rocks of the Valpelline Series (Dent-Blanche Tectonic System, Western

17 Alps). Conventional structural analysis is integrated with the extraction of structural data from 3D

18 models of representative smooth outcrops. Quantitative microstructural and mineral-chemical

19 analyses are combined to link structural and metamorphic evolution. This approach allows

20 identifying and correlating foliations that developed during three tectono-metamorphic stages. The

21 first (D_1) includes solid-state deformation associated with an early foliation (S_1) preserved within

22 metabasite boudins enclosed in migmatite gneiss. The second (D_2) is related to the dominant foliation

23 in migmatite gneiss (S_2), coeval with the regional scale anatexis and growth of garnet and cordierite.

24 The third (D_3) is related to the late folding of S_2 and the development of a sillimanite-rich axial plane

25 foliation (S_3) which wraps around garnet and cordierite. Finally, this work discusses pros and cons of

26 each innovative methodology, still emphasising the importance of using manual field data as ground

27 control.

1. Introduction

29 In the last two decades, new methods including remote sensing techniques and on-field data

30 acquisition using smartphones and tablets (e.g., Lee et al., 2013; Field-Move app; Midland Valley,

31 2015), are changing the way geoscientists collect data in the field (e.g., Zerboni et al., 2015; Tavani

32 et al., 2022; Misra and Mukherjee, 2023). In particular, there is a growing accessibility to high-

33 resolution satellite imagery (e.g., Perego et al., 2011), and it is relatively easy to acquire

34 photogrammetric images using different instruments. These range from digital cameras equipped with

35 LiDAR (Laser Imaging Detection and Ranging) sensors to UAVs (Unmanned Aerial Vehicles). The

36 development of relatively small and low-cost UAVs permits the high-resolution mapping of areas

37 and their 3D reconstruction, especially when no LiDAR data can be retrieved (e.g., Forti et al., 2023).

38 One of the most common techniques of digital photogrammetry is the Structure from Motion (SfM),

39 which permits to reconstruct a 3D structure from bidimensional photographs. The 3D models

40 obtained by these techniques encompass valuable data for structural geology (e.g., Tavani et al., 2014;

41 2016; Cawood et al., 2017; Mattéo et al., 2021), geomorphology (Bonasera et al., 2022, 2023; Misra

42 and Mukherjee, 2023), and archaeometry (Brandolini et al., 2020). All these approaches are

43 particularly effective in Alpine environments undergoing deglaciation, where the absence of

44 vegetation cover and the smoothness of the outcrops permit a clear exposure of rocks and structures.

45 Many studies used these techniques to extract structural data such as orientations of foliation surfaces,

46 fold axes, and fractures. The results remain reliable even when compared to handheld measured data,

47 typically exhibiting a mismatch of approximately 5° in dip values and 10°–15° in dip azimuth (e.g.,

48 Cawood et al., 2017; Novakova and Pavlis, 2017). This approach may be particularly useful in such

49 environments where obtaining a statistically significant number of orientations for structural

50 calculations (e.g., fold analysis, fractures analysis; Ramsey and Huber, 1987; Cawood et al., 2017)

51 may be complex due to several factors. These include (i) the geographical location of the outcrops at

52 high altitudes and/or with snow coverage, making them accessible only for a few months during the

53 year and only a few hours a day; (ii) outcrops located on vertical cliffs that are completely inaccessible

54 for traditional data measurements and sampling. In these situations, aerial photogrammetry with

55 drones and/or 3D outcrop modelling through cameras equipped with LiDAR sensors are very helpful.

56 Indeed, this approach allows also to extend the dimensions of the study area up to the hectometer

57 scale.

58 In the last years, several innovative methodologies have been also improved for microstructural and

59 mineral-chemical analysis of crystalline basements (e.g., Corti et al., 2019; Visalli et al., 2021; Zucali

60 et al., 2021; Caso, 2023; Fazio et al., 2024) that are facilitating the quantitative digital transition of

61 fabric and petrological rock parameters acquisition. These techniques include the extraction of

62 quantitative grain shape parameters from thin sections by semi-automatic segmentation (Heilbronner,

63 2011; Heilbronner and Barrett, 2014; Corti et al., 2019; Visalli et al., 2021) and quantitative chemical

64 data extraction from Electron MicroProbe Analyser (EMPA) X-ray maps and point mineral-chemical

65 analyses (e.g., XMapTools; Lanari et al., 2014; Q-XRMA; Ortolano et al., 2018). The combination

66 of these two techniques is effective in discriminating different generations of superimposed structures

67 and defining tectono-metamorphic stages (e.g., Corti et al., 2019; Roda et al., 2021; Zucali et al.,

68 2021; Caso, 2023).

69 The goal of this work is to combine these analysis techniques developed to operate at different scales.

70 Indeed, a reliable reconstruction of the tectono-metamorphic evolution of crystalline basements

71 requires a multiscale approach to collect and analyse structural data, specifically foliations and folds

72 associated with superimposed deformation stages. In this situation, is also fundamental the

73 identification of the mineral assemblages supporting each structure (e.g., Spalla, 1993; Johnson and

74 Vernon, 1995; Zucali et al., 2002; Passchier and Trouw, 2005; Spalla et al., 2005). Moreover, these

75 techniques aid in the targeted choice of meso- and microstructural domains with different deformation

76 and metamorphic transformation degrees (e.g., coronitic, tectonitic and mylonitic domains; Salvi et

77 al., 2010; Gosso et al., 2015; Zucali et al., 2020), aimed at reconstructing the whole tectono-

78 metamorphic history.

79 The use of modern quantitative techniques may be particularly useful in the study of migmatitic

80 basement rocks, characterised by complex structural patterns derived from the interplay between

81 metamorphic, magmatic, and deformative processes under transient conditions (Brown, 1973;

82 Hopgood, 1979; Ashworth, 1985; Kreigsman, 2001; Sawyer, 2001, 2008; Kreigsman and Alvarez-

83 Valero, 2010; Yakimchuk, 2020). In fact, multiple partial melting events and the complex geometrical

84 patterns resulting from melt migration (Sawyer, 2001) complicate the reconstruction of the tectono-

85 metamorphic evolution of these basements. Consequently, it is often difficult to reconstruct the

86 relative chronology of the deformation events during high-temperature (HT) evolution through

87 traditional "field-based only" structural analysis. However, a multidisciplinary and multiscale

88 approach that combines meso- and microscale analysis supported by mineral-chemical data using

89 different new approaches is still missing.

90 Therefore, in this study, we choose the migmatitic basement of the Valpelline Series (Dent-Blanche

91 Nappe, Western Italian Alps) as a case study, to envisage a comprehensive view of its structural and

92 tectono-thermal evolution. This series represents a fragment of the pre-Alpine lower continental crust

93 that underwent HT deformation and partial melting during Permian lithospheric extension (Zucali et

94 al., 2011; Pesenti et al., 2012; Manzotti and Zucali, 2013, Caso, 2023; Caso et al., 2024).

2. Geological setting

96 The Alps (Fig. 1a) are one of the peri-Mediterranean mountain ranges originated from the subduction

97 of the Ligurian-Piedmont Ocean during the Cretaceous and collision between the Adria and European

98 plates in the Eocene (Dewey et al., 1989; Schmid et al., 2004; Beltrando et al., 2010; Handy et al.,

99 2010; Lardeaux, 2014; Angrand and Mouthereau, 2021). The Austroalpine and Penninc domains

4

100   constitute the axial zone of the Alps, whose oceanic and continental rocks underwent high-pressure

101   and low-temperature metamorphism during the Alpine subduction.

102   The Dent-Blanche Tectonic System (DBTS; Manzotti et al., 2014a; Manzotti and Ballèvre, 2017)

103   belongs to the Austroalpine domain and overlies the oceanic units. The DBTS is traditionally divided

104   into the Dent-Blanche s.s. to the northwest and the Mont-Mary Nappe to the southwest separated by

105   a km-scale mylonitic zone, the Roisan-Cignana Shear Zone (RCSZ, Fig. 1b; Zucali et al., 2011;

106   Manzotti et al., 2014a, b). The Dent-Blanche s.s consists of a Paleozoic basement corresponding to

107   the Arolla and the Valpelline series (Diehl et al., 1952; Manzotti and Zucali, 2013; Manzotti et al.,

108   2014a) which recorded both pre-alpine and alpine metamorphism. The Arolla Series is made of

109   Permian metagranitoid, metagabbro and pre-Permian lenses of migmatite gneiss. Alpine

110   metamorphism and deformation are more pervasive in the Arolla Series than in the Valpelline Series.

111   In particular, in the Arolla Series the Alpine metamorphism developed under blueschists-facies

112   conditions (Roda and Zucali 2008; 2011; Manzotti et al., 2014a, b; Manzotti et al., 2020). Conversely,

113   the Valpelline Series (VP) better preserves Permian structures and metamorphic assemblages (Zucali

114   et al., 2011; Pesenti et al., 2011; Kunz et al., 2018) from the amphibolite- to granulite-facies

115   conditions (Gardien et al., 1994; Manzotti and Zucali, 2013; Caso, 2023; Caso et al., 2024).

116   *Insert Figure 1 here.*

117   The VP consists of migmatitic metapelites, as Grt–Crd- (abbreviations hereafter are according to

118   Whitney & Evans, 2010) and Grt–Opx-migmatite gneiss, and sillimanite-gneiss, plus felsic granulite.

119   Metasedimentary and felsic rocks are associated with Grt–Cpx-amphibolite also locally affected by

120   partial melting (black amphibolite in Fig. 2a), minor pegmatites and aplites, basic granulites and

121   marbles (Diehl et al., 1952; Nicot, 1977; Gardien et al., 1994; Manzotti and Zucali, 2013; Caso et al.,

122   2024). In the VP a former tectono-metamorphic stage (pre-D_2 in Manzotti and Zucali, 2013) is marked

123   by a relict foliation preserved in meter-scale metabasite bodies. This stage has developed at $T =$

124   $700\pm50°C$ and $P = 0.57\pm0.11$ GPa (Manzotti and Zucali, 2013). Conversely, Gardien et al. (1994)

125   estimated higher pressure conditions within the kyanite stability field (T = 700–800°C and P = 0.9–

126   1.0 GPa) for the pre-D$_2$ stage preserved within garnet cores. D$_2$ stage is related to the development of

127   the regional foliation S$_2$ and widespread melting, at T = 810±40°C and P = 0.7±0.01 GPa (Gardien et

128   al. 1994; Manzotti and Zucali, 2013). S$_2$ is parallel to the lithological boundaries and strikes NE–SW

129   dipping at high angles. During a later stage (T = 800±30°C and P = 0.6±0.07 GPa; D$_3$ in Manzotti

130   and Zucali, 2013), the S$_2$ is folded, leading to the local development of an S$_3$ axial plane foliation,

131   marked by the blastesis of biotite and sillimanite both at the meso- and microscale. Gardien et al.

132   (1994) recognised a further migmatitic stage related to the cordierite growth, estimated at T = 650–

133   700°C and P = ~0.35–0.45 GPa. However, recent microstructural analyses found the presence of

134   cordierite within melt-rich portions developed during D$_2$ and wrapped by S$_3$ sillimanite-rich foliation

135   (Caso et al., 2024).

136   The Alpine deformation in the VP is localized in decameter- to hectometer-wide shear zones (crossed

137   patterns in Figure 2a) marked by cataclasites and mylonites (Pennachioni and Guermani, 1993; Roda

138   and Zucali, 2008; Manzotti and Zucali, 2013). The mylonitic foliation is marked by chlorite and white

139   mica and developed under greenschists-facies conditions (T = 430±30°C and P = 0.3–0.5 GPa;

140   Gardien et al., 1994; Manzotti and Zucali, 2013). Mylonitic rocks occurring at contact with the Arolla

141   Series may be contemporaneous to the RCSZ shearing, under blueschists-facies conditions (D$_3$-D$_4$

142   stages in Manzotti et al., 2014b). Late stages of Alpine deformation (see D$_5$ stage in Manzotti et al.,

143   2014b) may be also responsible for the change in orientations of pre-Alpine S$_2$ and S$_3$ foliations in

144   the VP, approaching Arolla Series and RCSZ (Dal Piaz et al., 2016; Manzotti et al., 2014b). The

145   precise age of the Alpine metamorphism in the VP is not well-constrained. The whole-rock Rb/Sr

146   ages of Alpine mylonites at the contact between the Arolla and Valpelline series are of ~57 Ma

147   (Angiboust et al., 2014).

148   *Insert Figure 2 here.*

149   **3. Methods**

150   *3.1 Mesoscale structural analysis*

151   Mesoscale structural analysis has been conducted by combining traditional field observations and

152   measurements with the extraction of data, from UAVs flights and LiDAR point clouds, of the main

153   fabric elements (foliations and dykes orientations). In particular, the orientations of foliations, aplites

154   and pegmatites have been firstly acquired with the compass on the field, together with rock sampling

155   of representative migmatite gneiss for a better constrain of the remote data acquisition. This approach

156   was used in clear and smoother outcrops which represent ideal case studies for 3D outcrop modelling.

157   SfM technique permitted to develop a 3D model of the selected areas in the VP from 2D images

158   georeferenced in WGS84 coordinates system retrieved with UAV (Westoby et al., 2012; Niedzielski,

159   2018). The area covered by UAV flight is approximately 40,000 m^2, located at the Lac Mort (see the

160   yellow square in Fig. 2a; coordinates: x: 382627; y: 5086138; z: 2850 m a.s.l.), on the right slope of

161   the Place Moulin creek Valley. Flights at 15 and 30 m height were made using a Parrot® Anafi drone

162   equipped with a 4k/21 MP camera (Fig. 3a), for the acquisition of ~380 photos, with a resolution of

163   5344*4016 pixels. After that, the photos have been uploaded in Agisoft Metashape version 1.5.5

164   software (Agisoft Metashape, 2023), and automatically aligned and processed to obtain a point cloud

165   and a mesh model.

166   Selected outcrops of this area have been scanned through an iPad 11'' Pro equipped with a LiDAR

167   sensor, using the 3D scanner App©, which directly produces a 3D model from a point cloud (Fig.

168   3b). Both the point clouds derived from the SfM and LiDAR scanning have been exported,

169   reprojected in coordinate metric system (WGS84 – UTM32N) and processed within the

170   CloudCompare software version 2.13 (CloudCompare, 2023), to extract the orientation of the main

171   structural elements. The CloudCompare *Compass* plug-in (Thiele et al., 2017) permits tracing the

172   upper and lower boundaries of a structural element (e.g., including dykes and layers) and produces

173   an interpolated plane that has its dip direction and dip angle (Fig. 3c). Then, the so-obtained structural

174   data were extracted from the software and projected on equal areal stereo plots, together with compass

175 measures, to increase the total number of available structural data and using manual measures as

176 ground control.

177 The traces of dykes visible from the Google Satellite© imagery were traced and grouped in a vector

178 polyline layer (Fig. 3d), and processed through the *Qgsurf* plug-in

179 (https://gitlab.com/mauroalberti/qgSurf) in QGIS version 3.22 (QGIS Development Team, 2023).

180 This tool, using the DEM (Digital Elevation Model) as a base, allowed us to obtain the dip direction

181 and dip angle of a plane which represent the best fit of each traced line intersecting the topographic

182 surface. Then, the data were plotted in an equal areal stereo plot as strikes of the lines calculated from

183 the dip directions.

184 *Insert Figure 3 here.*

185   *3.2 Microscale structural analysis*

186 Two samples for quantitative microstructural analysis have been chosen after analysing at the optical

187 microscope dozens of different migmatite gneiss from different localities of the VP. The chosen

188 samples show different modal proportions, mineral phase distributions and structures. In particular,

189 one sample is representative of a melanosome, and one is representative of a leucosome (33SC and

190 VP34 respectively; see samples location in Fig. 2a), both corresponding to cordierite-migmatite

191 gneiss. First, they were analysed with the optical microscope for the reconstruction of the

192 microstructural relations between the different mineral phases, and to define the mineral assemblages

193 marking each recognised fabric element (Passchier and Trouw, 2005; Spalla et al., 2005). The

194 quantitative microstructural analysis was carried out through the Micro-Fabric Analyzer ArcGis

195 toolbox (MFA; Visalli et al., 2021; Fig. 4), used to obtain the vectorial contouring of the mineral

196 grains and measure their shape parameters (see Visalli et al., 2021 Appendix A for the explanation of

197 the calculated values).

8

198   In detail, the MFA toolbox comprises and uses: (i) the Grain Size Detector (GSD; Fig. 4) which traces

199   vectorial polygonal grains contouring maps by processing and segmenting a high-resolution optical

200   thin section scan (Fig. 4; Visalli et al., 2021); (ii) the Quantitative X-Ray Maps Analyzer tool (Q-

201   XRMA; Ortolano et al., 2018) which derived a mineral classification map obtained from X-ray maps

202   processing (first cycle); (iii) the Mineral Grain Size Detector (Min-GSD; Visalli et al., 2021) which

203   allows merging the outputs of the GSD and Q-XRMA to label each grain polygon feature with its

204   mineral phase name, since the GSD tool does not separate the grains into different minerals. To apply

205   the latter tool is necessary to geo-reference in ArcGIS the Q-XRMA output on the GSD one. Both

206   the MFA and Q-XRMA toolboxes have been developed at the Geoinformatics and Image Analysis

207   Lab of the Biological, Geological, and Environmental Sciences Department at the University of

208   Catania (Italy).

209   The thin section scans used in the GSD toolbox were acquired under crossed polarized light by using

210   an Epson V750 dual-lens system scanner at 24 bit-depth and 4800 dpi of resolution corresponding to

211   a pixel size of ~5.29 µm. These settings for this device represent the best compromise between high-

212   quality imaging, relatively fast image-processing time, and reasonable hard drive space storage

213   (Visalli et al., 2021).

214   Among the obtained shape parameters, the long axis orientation (values between $0° – 180°$) and the

215   roundness (see Supplementary Material 1 for all the obtained shape parameters) have been used for

216   the distinction of different microstructures marked by different mineral generations. In particular, the

217   long axis orientation is the angle between a vertical reference (in this case roughly perpendicular to

218   the main foliation of the thin section, depending on the thin section scan orientation) and the long

219   axis of each mineral grain, measured clockwise. Therefore, in this case, grains marking the main

220   foliation will have orientations of ~90°.

221   *3.2.1   Mineral-chemical analysis*

9

222 Quantitative mineral-chemical points analysis and X-ray chemical maps of major (Si, Ti, Al, Fe, Mn,

223 Mg, Ca, Na, K) and minor elements (Cr) have been acquired using the Electron Microprobe Analyser

224 (EMPA) JEOL 8200 Superprobe WDS at the Dipartimento di Scienze della Terra "A. Desio" –

225 Università degli Studi di Milano. For sample 33SC the Fe, Mg, Ti, Ca and Na maps were acquired

226 using five wavelength-dispersive spectometers (WDS) detectors, while Si, Al, Mn, Cr and K maps

227 using an energy-dispersive spectrometer (EDS) detector. These maps were acquired using a beam

228 current of 100 nA, with a dwell time of 55 ms and a resolution 1024*600 pixels (35 μm of step size).

229 For sample VP34 four element maps were acquired (Al, Fe, K, Na) using four WDS detectors. These

230 maps were acquired using a beam current of 50 nA, a dwell time of 15 ms and a resolution of

231 1024*512 pixels (pixel size of 35 μm). For quantitative mineral-chemical points analyses, an

232 accelerating voltage of 15 KeV and 50 nA of beam current was used. These were used as internal

233 standards in the Q-XRMA tool (second cycle; Ortolano et al., 2018; Corti et al., 2019; Roda et

234 al., 2021; Zucali et al., 2021; Caso, 2023) to obtain calibrated mineral maps showing the element

235 content (expressed in atoms per formula unit; apfu) for selected mineral phases (biotite and

236 garnet). By doing so, it was possible to highlight chemical variations and zoning within crystals

237 within different microstructural sites and use them to better constrain the tectono-metamorphic

238 evolution of the study area.

239 *Insert Figure 4 here.*

240 The tectono-metamorphic stages are named using a numerical progression (e.g., D_1, D_2, etc.). The

241 prefix D- stands for deformation, S- indicates foliations, A- fold axes, F- for folds, and A.P.- stands

242 for axial plane. Mineral formulae were calculated according to Deer et al. (1992) and using

243 pyMinColab v.2023 (Zucali, 2023).

244 **4. Rock types**

245 The Valpelline Series is mostly made by metapelites, including migmatite gneiss and sillimanite-

246 gneiss. Migmatite gneiss is the most common rock type and comprises both stromatic diatexites and

247   metatexites. Most migmatites are garnet-bearing, but in different localities of the valley cordierite–

248   garnet-bearing migmatite gneiss also occurs (see yellow stars in Figure 2a; Gardien et al., 1994;

249   Manzotti & Zucali, 2013; Caso, 2023; Caso et al., 2024). More rarely, garnet–orthopyroxene-bearing

250   migmatite gneiss are also found (see red star in Figure 2a; Caso et al., 2024). Sillimanite-gneiss and

251   minor felsic granulites occur as decametric to hectometric bodies interlayered with migmatite gneiss.

252   Metabasic rocks correspond to basic granulites and brown amphibolites occurring in meter-sized

253   lenses/boudins embedded in migmatite gneiss, and black amphibolite occurring as hectometric bodies

254   interlayered with metapelites, and locally affected by partial melting. Marble and calcsilicatic rocks

255   also crop out as hectometric bodies interlayered with metapelitic rocks and black amphibolites (Figure

256   2a; see Caso et al., 2024 for detailed lithological description).

257   In particular, in the Lac Mort area covered by LiDar and UAVs flights (Fig. 2a), two main groups of

258   lithologies occur: (i) basic granulite and brown amphibolite and (ii) cordierite-bearing migmatite

259   gneiss. In particular, the rocks of the former group crop out as meter-sized levels or boudins embedded

260   in the cordierite-migmatite gneiss (not mappable at the map resolution scale; Fig. 2a) and locally

261   folded.

262   Basic granulite shows a granoblastic to slightly gneissic fabric made by the isorientation of

263   orthopyroxene and clinopyroxene and minor whitish plagioclase-rich aggregates. Brown amphibolite

264   has a more pronounced gneissic structure made by the isorientation of brown amphibole and

265   millimetric plagioclase. Cordierite-migmatite gneisses here mainly correspond to metatexites,

266   showing a gneissic texture made by alternating leucosomes and melanosomes, which follows the

267   regional foliation trend and lithological boundaries. The paleosome locally occurs as fine-grained

268   pluridecimetric levels made of pyroxene, amphibole, biotite and plagioclase, similar to basic

269   granulites. Melanosomes include millimetric isoriented biotite and minor millimetric fibrous

270   sillimanite defining the main foliation. Leucosomes are made of fine-grained plagioclase, quartz and

271   locally minor K-feldspar. They show variable thickness, from centimetric to pluricentimetric,

11

occurring as regular levels parallel to the main foliation, locally folded, or plurimetric pods with

irregular shapes. Locally, a second generation of leucosome makes irregular patterns cross-cutting

the main fabric (the main melanosome-leucosome alternation parallel to the regional foliation).

Garnet occurs as millimetric to pluri-millimetric reddish porphyroblasts both in the melanosomes and

leucosomes, together with cordierite. The latter constitutes dark-grey porphyroblasts from pluri-

millimetric to centimetric. Within migmatites pluri-centimetric to metric lenses and boudins of fine-

grained migmatitic gneiss also occur. They have a granoblastic structure made of plagioclase, quartz

and minor garnet. Also, these portions, together with the migmatitic gneiss are cross-cut by

centimeter-thick and discordant leucosomes.

As stated above, cordierite-migmatite gneisses were detected in several localities of the VP (see

yellow stars in Fig. 2a). Nevertheless, it is hard to find fresh cordierite crystals within collected rock

samples suitable for reliable microstructural investigation and mineral analysis at the EMPA. Indeed,

most of the recognised cordierite blasts in thin sections are characterised by local or complete

transformation into fine-grained white mica or chlorite aggregates (Fig. 5) during late retrogression

(pinitisation; Schreyer and Seifert, 1970; Ogiermann and Kalt, 2000). The two selected samples

analysed in this work have been chosen from the Comba Vessonaz area (red dots in Fig. 2a) since

they show freshly preserved cordierite. Sample VP34 is representative of a melt-rich portion, while

the 33SC shows a well-developed sillimanite-rich foliation suitable for microstructural constraints.

Samples collected at the Lac Mort area (where the mesostructural study has been carried out) showed

strongly retrogressed cordierite and were not homogeneous or suitable for the tectono-metamorphic

reconstruction.

Insert Figure 5 here.

5. Results

5.1 Traditional mesostructural analysis

296 Together with field observations, (Fig. 6) a number of 154 orientations of structural elements has

297 been derived from compass measurements (Fig. 7).

298 The S_1 foliation is the internal foliation of basic granulite and brown amphibolite boudins wrapped

299 by the S_2, locally geometrically discordant to the long axis of the boudin and S_2 (Fig. 6a). In particular,

300 at the mesoscale, S_1 has been detected in correspondence F_2 isoclinal folds, where this foliation is not

301 completely transposed (Figs. 6b). In the basic granulite boudins, S_1 is a layering marked by the

302 isorientation of pyroxene- and plagioclase-rich domains and by amphibole-rich and plagioclase-rich

303 domains in the brown amphibolites. S_1 dips mainly toward NE, with variable but relatively high dip

304 angles (Fig. 7a). The mean orientation from field data, calculated from the Kamb contouring is

305 164/55°.

306 S_2 foliation is penetrative in migmatite gneiss. It is defined by the alternation between melanosomes

307 and leucosomes, and by the isorientation of biotite and sillimanite. S_2 dips mainly toward the S–SE

308 with variable dip angles, which are locally sub-vertical. Locally it also dips toward the NW sub-

309 vertically (Fig. 7c). The mean orientation calculated from the Kamb contouring field data is 142°/54°

310 (dip direction and dip angles). A_2 axes, folding S_1, trend toward S–SW and plunge at 60–80°; A.P.$_2$

311 axial planes dip toward S–SE with almost sub-vertical dip angles (Fig. 7e). S_2 is widely deformed

312 and folded by isoclinal (Fig. 6c, d) to open (Fig. 6e) F_3 folds, locally asymmetric, with a W-vergence

313 (Figs. 6e). In correspondence with the isoclinal folds, S_2 and leucosomes are folded, and S_3 axial

314 plane foliation locally develops (Fig. 6d). S_3 dips toward SE, with relatively high dip angles (Fig. 7g).

315 Cordierite is also deformed in correspondence of fold hinges, here occurring as dark-grey aggregates

316 (Fig. 6c). Locally, centimetric-thick leucosomes cross-cut S_2 foliation, along the limbs of F_3 folds

317 (Fig. 6e). These leucosomes also cross-cut the basic granulite boudins, making "a-type" flanking

318 structures with a top-to-the W sense of shear, with the leucosomes behaving as a cross-cutting element

319 (CE; Hudleston, 1989; Mukherjee, 2014; Fig. 6f). The centimeter-thick leucosomes discordant to the

320 S_2 dip toward E–SE and WSW (Fig. 7f). In some outcrops the F_3 folding produces a crenulation

321 cleavage S_3 (Fig. 6g). A_3 fold axes trend toward the S and plunge at 50–88°; $A.P._3$ axial planes dip

322 toward the SE with dip angles ranging between ~45 and 75° (Fig. 7g). Kfs-Qz pegmatites and aplites,

323 with different orientations and crosscutting relationship with the above-described structures, occur.

324 The mineralogy between the different systems is the same. One system of dykes is parallel to the

325 migmatitic foliation S_2 and is locally affected by boudinage (Fig. 6h); two late systems with different

326 orientations cross-cut each other and the folded S_2 (Figs. 6h and i), striking NW–SE and NNW–SSE

327 (Fig. 7h, i), both with dip angles ranging approximately from 65° to 85° (Fig. 7i). Moreover, some of

328 these late dykes are also affected by open folds (Fig. 6h). Cross-cut relationships visible on the field

329 highlight that aplites and pegmatites striking NW–SE (red dotted line in Fig. 6i) have been emplaced

330 after those striking NNW–SSE (yellow dotted line in Fig. 6i).

331 *Insert Figure 6 here.*

332   *5.1.2 3D virtual-outcrop analysis*

333 A total number of 369 orientations have been extracted from remote sensing data (Fig. 7): in

334 particular, 25 from UAV-derived point clouds, 107 from LiDAR-derived point clouds both processed

335 in CloudCompare, and 209 from Google Satellite© using the *Qgsurf* plug-in within QGIS.

336 *Insert Figure 7 here.*

337 S_1 in basic granulite and brown amphibolite boudins has been traced and measured using the point

338 clouds derived from iPad LiDAR scanning. 32 planes have been extracted (black dots in Fig. 7b).

339 The extracted surfaces have a dip direction both toward S–SE and N–NE. The first extracted cluster

340 has a dip direction ranging from ~150° to ~190° and dip angles between ~55° and 88°; the second

341 one has a dip direction of ~350° or between ~5°–20° and two sub-clusters of dip angles, one more

342 sub-vertical and one between ~40° and 65° (Fig. 7b). Planes extracted from the point clouds partially

343 overlap those measured in the field: only the first cluster of orientations dipping toward S–SE is

344 coherent with field measurements (green squares in Fig. 7a). The pervasive foliation S_2 at the outcrop

345 scale has been extracted both from the LiDAR point clouds and the UAV-derived one. The surfaces

346 have a dip direction both toward NE and SE. The first denser cluster has dip directions ranging from

347 ~145° to 195° and dip angles between 20° and 60°; the second one has dip directions between 315°

348 and 360° and dip angles between 0° and 10°, with dip angles similar to the first cluster (Fig. 7d). S_2

349 orientations extracted from CloudCompare overlap only the cluster dipping toward the S. S_2

350 orientations extracted from UAV point cloud (black dots in Fig. 7d) partly overlap those from LiDAR

351 and field, but are more scattered, and with relatively lower dip angles. Axes and axial planes related

352 to the D_2 and D_3 folding have not been extracted from CloudCompare due to the relatively low

353 resolution of the point clouds and the 3D outcrop flat shape not permitting line measurements of the

354 axes. For leucosomes discordant to S_2, only strikes have been plotted since the low resolution of the

355 point clouds and the size of the object, the dip angles were scattered or wrong (Fig. 7f).

356 29 data of aplites and pegmatites directions visible from both the UAV and LiDAR point clouds have

357 been extracted. There are two main clusters of directions: (i) one strikes NW–SE and (ii) the second

358 strikes WNW–ESE (Figs. 7j, k). Minor clusters striking E–W and NE–SW have also been measured

359 from CloudCompare. The data extracted from the *Qgsurf* plug-in are more scattered and cover various

360 orientation strikes: the most frequent is the one striking ENE–WSW (Fig. 7l). The data extracted from

361 CloudCompare match better with those measured on the field with the compass.

362   *5.2 Traditional microstructural analysis*

363 Sample VP34 comes from a leucosome-rich portion. It is characterised by a gneissic structure mostly

364 made by pluricentimetric-thick leucocratic levels consisting of plurimillimeter quartz, K-feldspar and

365 cordierite and rare plagioclase alternating with few millimeter-thick sillimanite and biotite-rich

366 melanocratic domains (Fig. 8a). Millimeter-sized garnet porphyroblasts mostly occur in melanosome

367 and in minor amount in leucosome. Cordierite occurs within leucosomes as plurimillimeter-sized

368 porphyroblasts (Fig. 8a). 33SC sample comes from a melanosome and differs from the former for the

369 higher modal abundance of sillimanite, biotite and garnet. In this sample, the pervasive foliation is

15

370   made by millimeter-sized fibrous and prismatic sillimanite with minor biotite and ilmenite (Figs. 8b

371   and c). Leucosomes are thin, discontinuous and composed of millimeter-sized quartz and minor

372   plagioclase, without K-feldspar (Fig. 8c). Garnet occurs as plurimillimeter-sized and locally flattened

373   porphyroblasts wrapped by the main foliation. In this sample cordierite is mosly plurimillimeter-

374   sized, strongly fractured and locally pseudomorphed by fine white mica aggregates (Fig. 8c).

375   *Insert Figure 8 here.*

376   S_2 is marked by the SPO of sillimanite (Sil II), biotite (Bt II; Figs. 9a and 10) and ilmenite, alternating

377   with leucosomes, made of quartz (Qz II), K-feldpsar and plagioclase in sample VP34 (Fig. 9b).

378   Locally, minor deformations in Bt II crystals along S_2 are observed. Quartz grain size is variable,

379   from plurimillimeter ribbons to millimeter and sub-millimeter equant blasts. Coarse-grained quartz

380   ribbons are oriented marking the S_2 fabric (Fig. 9b). Plagioclase occurs as rare millimeter blasts in

381   the leucosomes of sample VP34 and in discontinuous millimeter-thin levels in sample 33SC, together

382   with quartz. S_2 in sample 33SC is preserved as fold hinges within microlithons of the locally spaced

383   S_3 (Figs. 9c, d). S_3 is well developed in this sample and is marked by sillimanite (Sil III), idiomorphic

384   biotite lamellae (Bt III) and ilmenite, wrapping both garnet and cordierite porphyroblasts (Figs. 9d,

385   e). Garnet in both samples hosts sub-millimeter inclusions of biotite (Bt I), sillimanite (Sil I), and

386   quartz blasts (Qz I), having a rounded shape, thus not in equilibrium with garnet (Figs. 9c, d, f).

387   Locally, sillimanite inclusions align in the rim of the garnet making an internal foliation in continuity

388   with the external S_3 (Fig. 9f). Thus, garnet in sample 33SC grew from pre- to syn-kinematic (Passchier

389   and Trouw, 2005) with respect to S_3. Some of these syn-kinematic garnet porphyroblasts also have a

390   flattened shape (Figs. 8b, c and 9f). Fine-grained aggregates of white mica locally overgrow both

391   cordierite and K-feldspar. Quartz and biotite along S_3 foliation locally make intergrowths after garnet

392   (Qz III and Bt III).

393   *Insert Figure 9 here.*

394   *Insert Figure 10 here*.

395   *5.2.1   Quantitative microstructural analysis*

396   The Mineral-Grain-Size detector tool (Min-GSD) applied to both samples provided two vectorial

397   grain polygon maps whose grains are labelled with a mineral phase attribute (Figs. 11a and b). As a

398   result, the following rock-forming mineral grains have been distinguished in samples VP34 and 33SC

399   respectively: 1,125 and 15,058 sillimanite grains, 1,275 and 4,049 biotite grains, 112 and 1,277 garnet

400   grains, 2,092 and 757 white mica grains, 560 and 432 cordierite grains, 1,086 and 397 plagioclase

401   grains, 86 and 384 ilmenite grains, 1,929 and 311 quartz grains; in sample 33SC 127 chlorite grains

402   and 11 rutile grains occur. K-feldspar, detected only in sample VP34, has a number of 2,509 grains

403   (Fig. 11a). These values result in different modal percentages, obtained from the Q-XRMA first cycle

404   classification, highlighting huge differences mineral modes (Fig. 11c). Quartz + feldspars

405   (corresponding to leucosome) grains percentage differs in the two samples: in sample VP34 this sum

406   (quartz + K-feldspar + plagioclase) is relatively high (~70%) corresponding to 5,524 grains (yellow

407   grains in the right of Figure 11a); in sample 33SC quartz + plagioclase sum is much lower,

408   corresponding only to ~5% vol with 708 total grains (yellow grains in the bottom of Figure 11b).

409   Accordingly, biotite + sillimanite grains percentage (corresponding to the melanosome) is higher in

410   sample 33SC (~70%) and lower in VP34 (~10%). The same is for garnet which is more abundant in

411   sample 33SC (Fig. 11c).

412   *Insert Figure 11 here.*

413   Grain orientations data have been extracted from each mineral phase to check whether a link between

414   their orientations and the foliation they mark occurs. In particular, the MFA calculates the long axis

415   orientation angle (0–180°) measured clockwise from a reference vertical axis. The long axis

416   orientation values are clustered at ~ 90° for biotite, sillimanite, ilmenite and quartz (Fig. 12a). In

417   detail, biotite, sillimanite and ilmenite long axis orientations mostly have values of ~90°, with two

418   minor clusters at ~ 60° and ~120° for both samples. In sample VP34, all phases also show a

419   pronounced cluster between 60° and 90°, reflecting the local anastomosed geometry of S_2 foliation.

420   There is a relatively small number of grains with long axis orientation at 0° or 180°, and these

421   occurrences are more common in the sample 33SC. Garnet orientations have been plotted only for

422   sample 33SC, where, despite exhibiting more dispersion compared to other mineral phases, they show

423   a weak clustering of orientations at ~ 90° (Fig. 12a). Similarly, this pattern emerges for K-feldspar

424   found exclusively in sample VP34, where a slight clustering around 90° is observed (Fig. 12a).

425   The long axis orientation data is easily observed through orientation maps extracted from ArcGIS

426   (Figs. 12b, c, d, e, f, g). S_2 in sample VP34 is defined by the sillimanite and biotite grains whose long

427   axes have orientations between ~60° and 110° (Figs. 12b and c). Quartz and K-feldspar long axis

428   orientations in the leucosome, with angles comprised between ~60° and 110° (light blue and

429   yellowish shades; Figs. 12d and e), also support S_2.

430   Looking at sillimanite long axis orientation maps for sample 33SC (as already shown in Caso, 2023),

431   the grains having orientation at ~ 90° are those marking the main S_3 foliation (Figs. 12f, g). Grains

432   having various orientations, such as 0–30° (light-blue shades) or 130–180° (reddish shades; Figs. 12f

433   and g) mark S_2 in the microlithons (see zoom rose diagram and map in Fig. 12g). Also, some of more

434   scattered orientations not directly correlated with S_2 may be represented by grains included within

435   garnet.

436   *Insert Figure 12 here.*

437   Quartz and K-feldspars grains locally show SPO in sample VP34, marking S_2 foliation. This is

438   constrained through the roundness parameter (calculated as the width/lenght ratio of each grain) of

439   these two mineral phases (Figs. 13a, b). Quartz marking S_2 corresponds to grains with roundness

440   between 0.19 and 0.53 (yellow-orange grains in Fig. 13a). Purple and blue grains correspond to those

441   whose roundness is closer to 1 and are not suitable for marking S_2 (Figs. 13b and c). As shown in the

442   rose diagram for sample 33SC, a huge number of garnet grains has long axis with orientation at ~ 90°

443   (Fig. 12a), parallel to the main S_3 foliation (yellow, green, and orange grains in Fig. 13d). In this case,

444   the roundness parameter of garnet is often lower than 1 (yellow to orange grains; Figs. 13e, f). This

18

445 is in accordance with the flattened shape of the grains, making them suitable for marking S3 foliation

446 (Figs. 13e, f).

447 *Insert Figure 13 here*

448 **6. Quantitative mineral-chemical analysis**

449 Mineral-chemical analysis on sample 33SC was carried out on biotite and garnet by Caso (2023)

450 using a different software. Here we used the Q-XRMA second cycle to obtain biotite and garnet-

451 calibrated maps, extending the comparison with EMPA point analyses and deeply discussing the

452 results.

453 Mg, Fe and Ti calibrated maps were analysed to check biotite chemical variations. The Mg content

454 in biotite varies from 2.39 to 3.24 apfu (Fig. 14a). Fe varies from 1.50 to 2.20 apfu (Fig. 14b), resulting

455 in Mg# (Mg/Fe+Mg) from ~0.5 to 0.7 (Fig. 14c). Mg increases toward the core and is higher in the

456 biotite grains in the garnet strain shadows (Fig. 14a). Conversely, Fe is higher in biotite grains

457 included within garnet porphyroblasts, at the rim of the grains marking the S3 foliation and in biotites

458 replacing cordierite (Fig. 14b). The Ti content ranges from 0.30 to 0.70 apfu (Fig. 14d) and is higher

459 in biotite grains included within garnet (Bt I) and increases in the core of some coarser biotite blasts

460 (Bt II). The lowest values are found in some biotites marking the main S3 foliation (Bt III), especially

461 in those growing after cordierite (Fig. 14d).

462 The Ti content of biotite has been used for calculating the temperatures through the Ti-in-biotite

463 thermometer of Henry et al. (2005). Considering only EMPA point mineral-chemical data (pink

464 symbols in Fig. 14c), the *T* ranges between 730 and 800°C; using Ti content extracted from each pixel

465 of the calibrated map, the *T* range becomes wider, with a mean cluster between 650 and 800°C.

466 Garnet has already described in Caso (2023) and is mostly homogeneous. It shows only a weak

467 zonation for Ca, thus with increasing grossular component toward the rim. Mg and Fe apfu, as visible

468 from calibrated maps, are homogeneous with a slight variation toward the rim, especially when in

19

469   contact with biotite (Figs. 14e, f). Mg is mostly between 0.77–0.80 apfu, up to decreasing at 0.69 in

470   the rim in contact with biotite (Fig. 14e). Fe is homogeneous in most of the blasts, being 2.13 apfu,

471   up to 2.22 in the rim in contact with biotite (Fig. 14f). All chemical data obtained by the EMPA and

472   extracted from each pixel of the calibrated maps are reported in Supplementary Material 2.

473   *Insert Figure 14 here.*

474   **7. Discussions**

475   *7.1 Tectono-metamorphic evolution of the Valpelline Series*

476   The multiscale and multi-method structural analysis allowed the definition of three tectono-

477   metamorphic stages in the Valpelline Series, namely D_1, D_2 and D_3 (Fig. 15).

478   D_1 is testified by the S_1 foliation, preserved mostly in basic granulite and brown amphibolite boudins

479   and locally discordant to the external S_2 (Figs. 6a, b and 15). S_1 dips mainly toward the SW with

480   scattered dip angles. At the microscale, in metabasic rocks, this foliation is defined by the alignment

481   of clino- and orthopyroxene, brown amphibole, plagioclase and in minor amounts biotite and

482   orthoamphibole (see Caso et al., 2024 for details about D_1). In migmatite gneiss is harder to constrain

483   the D_1: the round-shaped inclusions of Bt I, Sil I, and Qz I within garnet or cordierite may be both

484   remnants of the D_1 stage in the hosting migmatitic gneiss or just inclusions from the D_2 stage.

485   Extracted quantitative parameters for the rock-forming mineral phases support the above-described

486   relationships: part of biotite, sillimanite and quartz grains with long-axis orientations diverging from

487   the main foliation (Fig. 12a) can be ascribed to Bt I, Sil I and Qz I grains included within garnet and

488   cordierite which show no preferred orientation. Nevertheless, this parameter alone is not sufficient

489   for this constrain; most of these grains have a round shape, rarely elongated, corresponding to grains

490   with roundness (w/l) parameter closer to 1 (e.g., quartz data in purple and blue in Figures 13c).

491   Mineral-chemical variations are not strongly enough to constrain these relationships, since H*T*

492   metamorphism often led to chemical homogenisation during cooling. However, only Bt I included

20

493   within garnet locally preserve chemical variation, thus being characterised by the highest Ti values

494   (0.5–0.7 apfu; Figs. 14c and d), resulting in higher calculated temperature up to ~800 °C (Fig. 14d).

495   During this stage S_1 is deformed and S_2 axial plane foliation develops. S_2 is characterized by the

496   alternation between melanosomes and leucosomes within migmatite gneisses. S_2 dips toward the SW,

497   with high dip angles. At the microscale, S_2 is well-developed in sample VP34 and is highlighted by

498   SPO of sillimanite and biotite (Sil II and Bt II) in the melanosomes and SPO of quartz (Qz II) and K-

499   feldspar in the leucosomes. Quartz grains highlighting S_2 in sample VP34 (Qz II) are those having a

500   relatively low roundness parameter, due to their elongated shape (Figs. 13a, c). The long axis

501   orientations with a main cluster oriented at ~90°, extracted through the MFA tool for these mineral

502   phases highlight S_2. Long axis orientations at 30° and 120° support the presence of Bt II highlighting

503   the remnants of the S_2 within the microlithons of sample 33SC. Locally within these domains, larger

504   deformed Bt II grains show a relatively high-Ti content (~0.5 to 0.7 apfu; Figs. 14c and d).

505   Leucosome percentage (quartz + plagioclase + K-feldspar), estimated at the microscale through the

506   MFA, may give an idea of the amount of melt present within the studied rock volume, in this case

507   higher in sample VP34 (Fig. 11a). However, leucosome does not always represent the melt-fraction

508   (e.g., Lee et al., 2020) or it can easily escape during brittle or shear deformation (Sawyer, 2001;

509   Etheridge et al., 2021; Daczko & Piazolo, 2022). Moreover, it can also be possible that some of the

510   K-feldspar or plagioclase blasts occurring within leucosomes represent solid peritectic products of

511   biotite-dehydration melting reaction (Le Breton & Thompson, 1981; Spear, 1994; Waters, 2001;

512   White et al., 2014) and not always something crystallised directly from the melt. Nevertheless, in

513   these samples and in others of the VP, several melt-bearing microstructures have been recognised

514   (Caso et al., 2024), such as melt films among grain boundaries or back-reaction structures after melt

515   consumption (e.g., biotite-quartz intergrowths; Sawyer, 2008; Kreigsman & Alvarez-Valero, 2010),

516   related to the D_2-D_3 stages. It is harder to estimate how much melt has been produced in sample 33SC:

517   this may represent a situation where most of melt has escaped from the rock volume or has been

518 consumed during back-reaction involving peritectic phases and melt, producing biotite and

519 sillimanite.

520 Garnet and cordierite, which occur within leucosomes formed during D_2, represent peritectic phases,

521 according to the Bt + Sil + Qz + Pl = Grt + Crd + Kfs + melt reaction (Kreigsman and Alvarez-Valero,

522 2010; Waters, 2001; White et al., 2014). The mutual relationship between garnet and cordierite is not

523 easy to constrain; however, both are wrapped by S_3 sillimanite-biotite foliation, constraining their

524 growth during the D_2 (see also Caso et al., 2024).

525 Garnet growth relations during the partial melting evolution are difficult to reconstruct using mineral-

526 chemical criteria; these are homogenous and show almost no chemical zoning, apart from weak

527 zoning of Fe and Mg toward the edge in contact with biotite, due to late diffusional resetting during

528 cooling. This is also testified by temperatures obtained in these rocks using the Grt-Bt exchange

529 thermometer: temperatures go down to 650°C (Caso et al., 2024).

530 During D_3, S_2 is deformed with open to isoclinal folds, with the local development of the sillimanite-

531 rich S_3 foliation (Figs. 6c, d, e, f and 15). During this stage, leucosomes and cordierite are deformed.

532 This is more evident at the mesoscale, where dark-grey aggregates of cordierite are folded and

533 concentrated in the fold hinges (Figs. 6d and 15).

534 At the microscale, S_3 is well observable in sample 33SC and it is marked by the SPO of sillimanite

535 and biotite. The long axis orientations with a main cluster oriented at ~90°, extracted from MFA tool

536 for sillimanite, biotite, and ilmenite refer to S_3 (i.e., Sil III and Bt III). Even though garnet grows

537 during D_2 it continues its crystallisation during the early D_3. Quantitative MFA data of garnet

538 demonstrate the presence of flattened porphyroblasts corresponding to those having a roundness

539 locally strongly < 1 (Fig. 13e, f). Bt III corresponds to grains having a lower Ti content with respect

540 to Bt I and Bt II, ranging from ~0.3 to 0.5 apfu and thus yielding slightly lower temperatures between

541 ~650–730 °C (Fig. 14d).

542 The two analysed samples are representative of different stages of the partial melting history of the

543 VP: indeed, sample VP34, which corresponds to a cordierite-bearing leucosome (Fig. 12a), is

544 representative of melt production during D_2, since its main foliation corresponds to S_2. Conversely,

545 sample 33SC is almost devoid of leucosomes, apart from rare millimeter-thin levels, and is strongly

546 enriched in sillimanite and biotite that mark S_3 foliation, with S_2 preserved in few microdomains as

547 relict fold hinges. Thus, this sample may represent the melt-consuming reactions during D_3, where

548 such a high modal amount of sillimanite can be produced by garnet or cordierite back-reacting with

549 melt, giving Sil III and Bt III (Spear, 1994; Kreigsman and Alvarez-Valero, 2010). Meanwhile, is

550 also possible that part of melt has escaped from this rock during D_3, migrating toward low-strain

551 zones where the S_2 fabric is well-recognisable.

552 Geometrical overprinting relationships between different systems of aplite and pegmatite dykes,

553 which widely intrude into the migmatr gneiss, allowed to divide the D_3 into an early and late D_3 stage

554 (Fig. 15). One system of dykes parallel to the S_2 and locally affected by boudinage (Fig. 6h) may

555 have intruded gneiss during the D_2 or early D_3 stage. Then, other systems of dykes intruded

556 migmatites by cross-cutting the syn-D_2 and syn-D_3 foliations and folds (Figs. 6h, i). Moreover, part

557 of these dykes cross-cutting D_3 folds, and striking NNW-SSE are also locally affected by open folds

558 (Fig. 6h), probably developed during the ongoing deformation during early D_3 (Fig. 15). It is possible

559 that dykes started intruding migmatites during late stages of D_2, using the S_2 foliation as preferential

560 path or weakness layer, being progressively affected by boudinage during progressive deformation;

561 then, during D_3 folding, some intruding dykes are folded. In the latest stages of D_3, dykes intruded

562 migmatite gneiss, crosscutting all structures ($D_2 + D_3$) without being further deformed.

563 *Insert Figure 15 here.*

564   *7.2 Pros and cons of quantitative multiscale structural analysis*

565   The multiscale digital acquisition methods used in this work have given an interdependent picture of

566   the reconstructed sequence of deformation events (Fig. 15). This allowed also to better constrain the

567   paragenetic sequence on which the thermodynamic calculations are usually based (Palin et al., 2016).

568   In particular, the quantitative mesoscale structural analysis made by the integration of traditional

569   compass measurements with data extracted from LiDAR sensor or UAVs-derived point clouds,

570   allowed to collect a statistically high number of structural data (in most cases more than ~50), even

571   from inaccessible outcrop portions. Nevertheless, there are still some structural artefacts resulting

572   from the use of CloudCompare on point clouds. In this case, the problems were eliminated by the

573   direct ground control carried out during the traditional survey campaign (i.e., comparison with

574   compass manual measurements of structural elements). Indeed, even though most of the S_1 and S_2

575   data extracted from CloudCompare fit well with the ones measured on the field (see Figs. 7a, b, c, d,

576   b), this software often extracts orientations having the same strike as those measured with the

577   compass, but with opposite dip directions. This can be explained by a difference in the dip angle of a

578   few degrees (5–10°) which apparently changes the dip direction of sub-vertical planes. However, this

579   misfit may derive from systematic errors during field-based data collecting, especially of sub-vertical

580   planes where the user is often led to make the planes dip toward the same direction. Moreover, as is

581   often the case, these artefacts can be also caused by: a) the low density of the point clouds useful for

582   reconstructing the 3D model; b) the presence of shadows during LiDAR or UAVs acquisitions; c)

583   flattened outcrop exposure leading to wrong plane interpolation and measure; d) the difficulty of

584   acquiring data in places that are too inaccessible leading to a low number of data to be used as ground

585   control. Although the technique still has some problems to overcome, it should be able to integrate

586   perfectly with the traditional methods used to date. Data extracted measuring the orientations of dykes

587   polylines traced on Google Satellite© in QGIS, are the most scattered. This dispersion probably

588   derived from artefacts and "holes" of the DEM itself, used by the *Qgsurf* plug-in to measure dip

589   directions and dip of a plane interpolated from the traced polyline. This problem should be overcome

24

590   in two ways: (i) using a higher resolution DEM, better though extracted from UAVs survey which

591   can have resolutions of few centimeters; (ii) by carefully excluding, using manual data as ground

592   control, orientations without a geological meaning. Nevertheless, this technique has the advantage of

593   being low-cost, since Google Satellite© and QGIS tools are freely available and do not require

594   expensive hardware to be used.

595   On the other hand, also conventional structural analysis, characterised by the manual collection of

596   structural data, is a process which may be susceptible to human errors and biases. Therefore, to obtain

597   an objective structural assessment, the integration of traditional methods and semi-automated

598   techniques is necessary to have a double-check of structural measurements and quantitively constrain

599   the polyphase deformation.

600   The possibility of storing vectorised, microstructure-derived large datasets subdivided by mineral

601   phase through the MFA toolbox, opens up the possibility of following the path of a true digital

602   transition of geo-petrostructural data system acquisition, possibly within a unique and interoperable

603   geological large data system (georeferenced GIS databases). However, these data may still be

604   somewhat cumbersome to obtain since it is necessary to acquire EMPA X-ray maps with adequate

605   resolution, resulting in high costs and time-consuming grain post-processing.

606   Nevertheless, these digital storing of microstructural data will open the possibility of better

607   interoperate with previously available datasets, allowing them to be integrated synergistically in a

608   broader sense.

8. Conclusions

610   This work described a multiscale approach that combines traditional field-based methods with

611   remote-sensing and quantitative techniques useful to investigate crystalline basements. In particular,

612   we have integrated traditional structural survey with the extraction of structural data from LiDAR

613   and UAVs-derived point clouds, and Google Satellite©. Using the point clouds and Google Satellite©

imagery, we extracted structural data also from steep inaccessible outcrop portions, extending the observation scale. This allowed for increasing the number of the main structural element orientations (foliations, leucosomes and dykes), using the manual field compass data as ground control. Traditional microstructural analysis was combined with the extraction of quantitative shape parameters from semi-automated grain digitisation, stored in a GIS database, allowing to constrain the structural evolution.

The provided quantitative multiscale structural analysis allowed the reconstruction of the tectono-metamorphic evolution of the migmatitic rocks in the Valpelline Series. In particular, three main tectono-metamorphic stages have been recognised, referred to the HT evolution of the VP crust during the Permian. D_1 is a solid-state tectono-metamorphic stage, testified by the S_1 foliation preserved in basic granulite and brown amphibolite boudins. D_2 is related to melt production and development of the regional S_2 foliation, garnet, and cordierite growth; early D_3 is characterised by folding of the S_2 and local development of S_3 sillimanite-rich melt-consuming foliation wrapping around garnet and cordierite porphyroblasts. Lastly, three systems of aplites and pegmatites intrude within migmatitic gneiss from early- to late D_3-stages, cross-cutting all the migmatitic structures.

The integration of traditional and innovative multiscale structural analysis has proven to be an efficient approach to ease the study of migmatitic crystalline basements, characterised by complex superimposed structures and different metamorphic assemblages.

Acknowledgements

References

Allmendinger, R.W., Cardozo, N.C., Fisher, D., 2013. Structural Geology Algorithms: Vectors & Tensors. Cambridge University Press, Cambridge, England.

Angiboust, S., Glodny, J., Oncken, O., Chopin, C., 2014. In search of transient subduction interfaces in the Dent Blanche–Sesia Tectonic System (W. Alps). Lithos 205, 298–321. https://doi.org/10.1016/j.lithos.2014.07.001

Angrand, P., Mouthereau, F., 2021. Evolution of the Alpine orogenic belts in the Western Mediterranean region as resolved by the kinematics of the Europe-Africa diffuse plate boundary. BSGF-Earth Sciences Bulletin 192(1), 42. https://doi.org/10.1051/bsgf/2021031

Ashworth, J.R., 1985. Migmatites. Glasgow and London (Blackie & Son Limited).

Beltrando, M., Compagnoni, R., Lombardo, B., 2010. (Ultra-) High-pressure metamorphism and orogenesis: An Alpine perspective. Gondwana Res. 18, 147–166. https://doi.org/10.1016/j.gr.2010.01.009

Bonasera, M., Cerrone, C., Caso, F., Lanza, S., Fubelli, G., Randazzo, G., 2022. Geomorphological and Structural Assessment of the Coastal Area of Capo Faro Promontory, NE Salina (Aeolian Islands, Italy). Land 1(7), 1106. https://doi.org/10.3390/land11071106

Bonasera, M., Petroccia, A., Caso, F., Cerrone, C., Gregorio, F., 2023. Integrated geomorphological and structural analysis of coastal cliffs: The case study of Capo Faro Promontory, NE Salina, Aeolian Islands, Italy. 2023 IEEE International Workshop on Metrology for the Sea; Learning to Measure Sea Health Parameters, MetroSea 2023 - Proceedings, 2023, 519–523. https://doi.org/10.1109/MetroSea58055.2023.10317191

Brandolini, F., Cremaschi, M., Zerboni, A., Degli Esposti, M., Mariani, G.S., Lischi, S., 2020. SfM-photogrammetry for fast recording of archaeological features in remote areas, in: Bagnasco G.,

662 Bortolotto S., Garzulino A., Marzullo M. (Eds.), Milano internazionale: la fragilità territoriale dei

663 contesti archeologici. Atti del Convegno Internazionale (Milano, 13 marzo 2019), «Archeologia e

664 Calcolatori», 31.2, 33–45. https://doi.org/10.19282/ac.31.2.2020.04

665 Brown, M., 1973. The definition of metatexis, diatexis and migmatite. Proceedings of the Geologists'

666 Association 84, 371–382. https://doi.org/10.1016/S0016-7878(73)80021-5

667 Cardozo, N., Allmendinger, R.W., 2013. Spherical projections with OSXStereonet. Comput. Geosci.

668 51, 193–205. https://doi.org/10.1016/j.cageo.2012.07.021

669 Caso, F., 2023. Quantitative combined multiscale structural and minero-chemical analysis to unravel

670 the tectono-metamorphic evolution of cordierite-migmatite gneiss from the Valpelline Unit (Dent-

671 Blanche Nappe, Western Italian Alps, Valle d'Aosta). Rend. Online Soc. Geol. It. 60, 2–10.

672 https://doi.org/10.3301/ROL.2023.20

673 Caso, F., Strambini, A., Zucali, M., 2024. Structural, lithostratigraphic and thermal features of a

674 Permian lower crust from the Western Italian Alps (Valpelline Series, Valle d'Aosta). Geological

675 Magazine, *in press*. https://doi.org/10.1017/S0016756824000037

676 Cawood, A.J., Bond, C.E., Howell, J.A., Butler, R.W.H., Totake, Y., 2017. LiDAR, UAV or

677 compass-clinometer? Accuracy, coverage and the effects on structural models. J. Struct. Geol. 98,

678 67–82. http://dx.doi.org/10.1016/j.jsg.2017.04.004

679 Corti, L., Zucali, M., Visalli, R., Mancini, L., Mohammad, S., 2019 Integrating X-ray computed

680 tomography with chemical imaging to quantify mineral re-crystallization from granulite to eclogite

681 metamorphism in the Western Italian Alps (Sesia-Lanzo Zone). Front. Earth. Sci. 7, 327.

682 https://doi.org/10.3389/feart .2019.00327

683 Dal Piaz, G.V., Bistacchi, A., Gianotti, F., Monopoi, B., Passeri, L., Schivo, A., 2016. Note

684 illustrative del F. 070 Monte Cervino della Carta geologica d'Italia alla scala 1:50.000. Memorie

685 Descrittive Carta Geologica D'Italia 101, 5–258.

686 Daczko, N.R., Piazolo, S., 2022. Recognition of melferite – A rock formed in *syn*-deformational high-

687 strain melt-transfer zones through sub-solidus rocks: A review and synthesis of microstructural

688 criteria. Lithos, 430–431,106850, https://doi.org/10.1016/j.lithos.2022.106850

689 Deer, W.A., Howie, R.A., Zussman, J., 1992. An introduction to the rock-forming minerals. John

690 Wiley and Sons, New York.

691 Dewey, J.F., Helman, M.L., Turco, E., Hutton, D.H.W., Knott, S.D., 1989. Kinematics of the western

692 Mediterranean, in: Coward, M.P., Dietrich, D., and Park, R.G., (Eds.), Alpine Tectonics, Geological

693 Society of London Special Publication 45, 265–283. https://doi.org/10.1144/GSL.SP.1989.045.01.15

694 Diehl, E.A., Masson, R., Stutz, A.H., 1952. Contributo alla conoscenza del ricoprimento della Dent

695 Blanche. Memorie degli Istituti di Geologia e Mineralogia dell'Università di Padova, 17, 1–52.

696 Etheridge, M.A., Daczko, N. R., Chapman, T., & Stuart, C. A. 2021. Mechanisms of melt extraction

697 during lower crustal partial melting. J. Metam. Geol. 39(1), 57–75,

698 https://doi.org/10.1111/jmg.12561

699 Fazio, E., Alsop, G.I., Nania, L., Graziani, R., Iaccarino, S., Montomoli, C., Carosi, R., Luzin, V.,

700 Salvemini, F., Gambino, S., Cirrincione, R., Mamtani, M.A., 2024. CPO and quantitative textural

701 analyses within sheath folds. J. Struct. Geol. 178, 105000. https://doi.org/10.1016/j.jsg.2023.105000ù

702 Gardien, V., Reusser, E., Marquer, D., 1994. Pre-Alpine metamorphic evolution of the gneisses from

703 the Valpelline Series (Western Alps, Italy). Schweizerische Mineralogische und Petrographische

704 Mitteilungen 74, 489–502.

705 Gosso, G., Rebay, G., Roda, M., Spalla, M. I., Tarallo, M., Zanoni, D., Zucali, M., 2015. Taking

706 advantage of petrostructural heterogeneities in subduction collisional orogens, and effect on the scale

707 of analysis. Per. Mineral. 84(3), 779–825. https://doi.org/10.2451/2015PM0452

708   Grasemann, B., Stüwe, K., Vannay, J-C., 2003. Sense and non-sense of shear in flanking structures.

709   J. Struct. Geol. 25, 19–34. https://doi.org/10.1016/S0191-8141(02)00012-3

710   Handy, M.R., Schmid, S.M., Bousquet, R., Kissling, E., Bernoulli, D., 2010. Reconciling plate-

711   tectonic reconstructions of Alpine Tethys with the geological- geophysical record of spreading and

712   subduction in the Alps. Eart Sci. Rev. 102, 121–158. https://doi.org/10.1016/j.earscirev.2010.06.002

713   Heilbronner, R., 2011. Distortion of orientation data introduced by digitizing procedures. J. Microsc.

714   149(2), 83–96. http://dx.doi.org/10.1111/j.1365-2818.1988.tb04566.x

715   Heilbronner, R., Barrett, S., 2014. Image Analysis in Earth Sciences. Springer Berlin, Heidelberg.

716   https://doi.org/10.1007/978-3-642-10343-8

717   Henry, B., Guidotti, C.V., Thomson, J.A., 2005. The Ti-saturation surface for low-to-medium

718   pressure metapelitic biotite: implications for geothermometry and Ti-substitution mechanisms. Am.

719   Mineral. 90, 316–28. https://doi.org/10.2138/am.2005.1498

720   Hopgood A.M. 1979. Polyphase fold analysis as a means of interpreting the deformational history of

721   migmatites. Geology 31, 109–110.

722   Hudleston, P.J., 1989. The association of folds and veins in shear zones. J. Struct. Geol. 11(8), 949–

723   957. https://doi.org/10.1016/0191-8141(89)90046-1

724   Johnson, S.E., Vernon, R.H., 1995. Inferring the timing of porphyroblast growth in the absence of

725   continuity between inclusion trails and matrix foliations: can it be reliably done? J. Struct. Geol.

726   17(8), 1203–1206. https://doi.org/10.1016/0191-8141(95)00021-5

727   Kriegsman, L.M., 2001. Partial melting, partial melt extraction and partial back reaction in anatectic

728   migmatites. Lithos 56(1), 75–96. https://doi.org/10.1016/S0024-4937(00)00060-8

729   Kriegsman, L.M., Alvarez-Valero, A.M., 2010. Meltproducing versus melt-consuming reactions in

730   pelitic xenoliths and migmatites. Lithos 116, 310–320, https://doi.org/10.1016/j.lithos.2009.09.001

731   Kunz, B.E., Manzotti, P., von Niederhäusern, B., Engi, M., Darling, J.R., Giuntoli, F. Lanari, P.,

732   2018. Permian high-temperature metamorphism in the Western Alps (NW Italy). Int. J. Earth Sci.

733   107, 203–229. https://doi.org/10.1007/s00531-017-1485-6

734   Lanari P., Vidal O., De Andrade V., Dubacq B., Lewin E., Grosch E.G., Schwartz S., 2014.

735   XMapTools: a MATLAB©-based program for electron microprobe X-ray image processing and

736   geothermobarometry. Comp. Geosci. 62, 227–240. https://doi.org/10.1016/j.cageo.2013.08.010

737   Lardeaux, J.M., 2014. Deciphering orogeny: a metamorphic perspective. Examples from European

738   Alpine and Variscan belts: Part I: Alpine metamorphism in the western Alps. A review. Bulletin de

739   la Société Géologique de France 185(2), 93–114. https://doi.org/10.2113/gssgfbull.185.2.93

740   Le Breton, N.L., Thompson, A.B., 1988. Fluid-absent (dehydration) melting of biotite in metapelites

741   in the early stages of crustal anatexis. Contribution to Mineralogy and Petrology 99, 226–237,

742   https://doi.org/10.1007/BF00371463

743   Lee, S., Suh, J., Park, H-d., 2013. Smart Compass-Clinometer: A smartphone application for easy

744   and rapid geological site investigation. Comp. Geosci. 61, 32–42.

745   http://dx.doi.org/10.1016/j.cageo.2013.07.014

746   Lee, A.L., Lloyd, G.E., Torvela, T., Walker, A.M., 2020. Evolution of a shear zone before, during

747   and after melting. J. Geol. Soc. 177(4), 738–751. https://doi.org/10.1144/jgs2019-114

748   Manzotti, P., Zucali, M., 2013. The pre-Alpine tectonic history of the Austroalpine continental

749   basement in the Valpelline unit (Western Italian Alps). Geol. Mag. 150, 153–172.

750   https://doi.org/10.1017/S0016756812000441

751   Manzotti, P., Ballèvre, M., 2017. Tectonic history of the Dent Blanche. Geological Field Trips and

752   Maps 9(2.1), 73 pp. https://doi.org/10.3301/GFT.2017.02

753   Manzotti, P., Ballèvre, M., Zucali, M., Robyr, M., Engi, M., 2014a. The tectonometamorphic

754   evolution of the Sesia–Dent Blanche nappes (internal Western Alps): review and synthesis. Swiss J.

755   Geosci. 107(2), 309–336. https://doi.org/10.1007/s00015-014-0172-x

756   Manzotti, P., Zucali, M., Ballèvre, M., Robyr, M., Engi, M., 2014b. Geometry and kinematics of the

757   Roisan-Cignana Shear Zone, and the orogenic evolution of the Dent Blanche Tectonic System

758   (Western Alps). Swiss J. Geosci. 107,23–47. https://doi.org/10.1007/s00015-014-0157-9

759   Manzotti, P., Ballèvre, M., Pitra, P., Benita Putlitz, P., Robyr, M., Müntener, O., 2020. The Growth

760   of Sodic Amphibole at the Greenschist- to Blueschist-facies Transition (Dent Blanche, Western

761   Alps): Bulk-rock Chemical Control and Thermodynamic Modelling. J. Petrol. 61(4).

762   https://doi.org/10.1093/petrology/egaa044

763   Mattéo, L., Manighetti, I., Tarabalka, Y., Gaucel, J.-M., van den Ende, M., Mercier, A., Tasar, O.,

764   Girard, N., Leclerc, F., Giampetro, T., Dominguez, S., Malavielle, J., 2021. Automatic fault mapping

765   in remote optical images and topographic data with deep learning. Journal of Geophysical Research:

766   Solid Earth 126, e2020JB021269. https://doi.org/10.1029/2020JB021269

767   Midland Valley, 2015. FieldMove User Guide.

768   Misra, A.A., Mukherjee, S., 2023. Atlas of Structural Geological and Geomorphological

769   Interpretation of Remote Sensing Images. Wiley and Sons.

770   https://onlinelibrary.wiley.com/doi/book/10.1002/9781119813392.7

771   Mukherjee, S., 2014. Review of the flanking structures in meso- and micro-scales. Geol. Mag. 151,

772   957–974. https://doi.org/10.1017/S0016756813001088

773   Nicot, E., 1977. Les roches meso et catazonales de la Valpelline (nappe de la Dent Blanche, Alpes

774   italiennes). PhD Thesis, Paris.

775   Niedzielski, T., 2018. Applications of unmanned aerial vehicles in geosciences: introduction. Pure

776   and Applied Geophysics 175, 3141–3144. https://doi.org/10.1007/s00024-018-1992-9

777   Novakova, L., Pavlis, T.L., 2017. Assessment of the precision of smart phones and tablets for

778   measurement of planar orientations: a case study. J. Struct. Geol. 97, 93–103.

779   http://dx.doi.org/10.1016/j.jsg.2017.02.015

780   Ogiermann, J., Kalt, A., 2000. Chemical Characterization of Cordierite Breakdown Products in

781   Gneisses and Migmatites of the Schwarzwald and the Bayerische Wald. Journal of Conference

782   Abstracts 5(2), 752.

783   Ortolano, G., Visalli, R., Gaston, G., Cirrincione, R., 2018. Quantitative X-ray Map Analyser (Q-

784   XRMA): A new GIS-based statistical approach to Mineral Image Analysis. Comp. Geosci. 115, 56–

785   65. https://doi.org/10.1016/j.cageo.2018.03.001

786   Passchier, C.W., Trouw, R.A.J., 2005. Microtectonics. Springer, Berlin, Heidelberg.

787   https://doi.org/10.1007/3-540-29359-0

788   Pennacchioni, G., Guermani, A., 1993. The mylonites of the Austroalpine Dent Blanche nappe along

789   the northwestern side of the Valpelline Valley (Italian Western Alps). Memorie di Scienze Geologiche

790   45, 37–55.

791   Perego, A., Zerboni, A., Cremaschi, M., 2011. Geomorphological Map of the Messak Settafet and

792   Mellet (central Sahara, SW Libya). J. Maps 7(1), 464–475. https://doi.org/10.4113/jom.2011.1207

793   Pesenti, C., Zucali, M., Manzotti, P., Diella, V., Risplendente, A., 2012. Linking U-Th-Pb monazite

794   dating to partial melting microstructures: Application to the Valpelline series (Austroalpine domain,

795   Western Alps). Rend. Online Soc. Geol. It. 22, 183–185.

796   Ramsay, J.G., Huber, M.I., 1987. The Techniques of Modern Structural Geology: Folds and

797   Fractures. Academic Press.

798 Roda, M., Zucali, M., 2008. Meso and microstructural evolution of the Mont Morion metaintrusives

799 complex (Dent Blanche nappe, Austroalpine domain, Valpelline, Western Italian Alps). Ital. J.

800 Geosci. 127, 105–23.

801 Roda, M., Zucali, M., 2011. Tectono-metamorphic map of the Mont Morion Permian metaintrusives

802 (Mont Morion - Mont Collon - Matterhorn Complex, Dent Blanche Unit), Valpelline - Western Italian

803 Alps. J. Maps **7**, 519–535. https://doi.org/10.4113/jom.2011.1194

804 Roda, M., Zucali, M., Corti, L., Visalli, R., Ortolano, G. Spalla, M.I., 2021. Blueschist mylonitic

805 zones accommodating syn-subduction exhumation of deeply buried continental crust: The example

806 of the Rocca Canavese Thrust Sheets Unit (Sesia-Lanzo Zone, Italian Western Alps). Swiss J. Geosci.

807 114, 6–39. https://doi.org/10.1186/s00015-021-00385-7

808 Salvi, F., Spalla, M.I., Zucali, M., Gosso, G., 2010. Three-dimensional evaluation of fabric evolution

809 and metamorphic reaction progress in polycyclic and polymetamorphic terrains: a case from the

810 Central Italian Alps. In: Spalla, M.I., Marotta, A.M., Gosso, G. (Eds.), Advances in Interpretation of

811 Geological Processes, 334, 173–187. https://doi.org/10.1144/SP332.11

812 Sawyer, E.W., 2001. Melt segregation in the continental crust: distribution and movement of melt in

813 anatectic rocks. J. Metam. Geol. 19, 291–309. https://doi.org/10.1046/j.0263-4929.2000.00312.x

814 Sawyer, E.W., 2008. Working with Migmatites. Short Course Series: Mineralogical Association of

815 Canada, volume 38. Quebec: Mineralogical Association of Canada.

816 Schmid, S.M., Fügenschuh, B., Kissling, E. Schuster, R., 2004. Tectonic map and overall architecture

817 of the Alpine orogen. Eclogae Geologicae Helvetiae 97, 93–117. https://doi.org/10.1007/s00015-004-

818 1113-x

819 Seifert, F., Schreyer, W., 1970. Lower temperature stability limit of Mg cordierite in the range 1-7

820 kbar water pressure: a redetermination. Contrib. Mineral. Petrol. 27, 225–238.

821 https://doi.org/10.1007/BF00385779

822 Spalla, M.I., 1993. Microstructural control on the P-T path construction in metapelites from the

823 Austroalpine crust (Texel Gruppe, Eastern Alps). Schweizerische Mineralogische und

824 Petrographische Mitteilungen 73(2), 259–275. https://doi.org/10.5169/seals-55573

825 Spalla, M.I., Zucali, M., Di Paola, S., Gosso, G., 2005. A critical assessment of the tectono-thermal

826 memory of rocks and definition of tectono-metamorphic units: evidence from fabric and degree of

827 metamorphic transformations. Geol. Soc. Spec. Publ. 243(1), 227–247,

828 https://doi.org/10.1144/GSL.SP.2005.243.01.16

829 Spear, F., 1994. Metamorphic Phase Equilibria and Pressure-Temperature-Time Paths. Mineralogical

830 Society Monographs, 799 pp.

831 Tavani, S., Granado, P., Corradetti, A., Girundo, M., Iannace, A., Arbués, P., Muñoz, J.A., Mazzoli,

832 S., 2014. Building a virtual outcrop, extracting geological information from it, and sharing the results

833 in Google Earth via OpenPlot and Photoscan: An example from the Khaviz Anticline (Iran). Comp.

834 Geosci. 63, 44–53, http://dx.doi.org/10.1016/j.cageo.2013.10.013

835 Tavani, S., Corradetti, A., Billi, A., 2016. High precision analysis of an embryonic extensional fault-

836 related fold using 3D orthorectified virtual outcrops: The viewpoint importance in structural geology.

837 J. Struct. Geol. 86, 200–210, http://dx.doi.org/10.1016/j.jsg.2016.03.009

838 Tavani, S., Billi, A., Corradetti, A., Mercuri, M., Bosman, A., Cuffaro, M., Seers, T., Carminati, E.,

839 2022. Smartphone assisted fieldwork: Towards the digital transition of geoscience fieldwork using

840 LiDAR-equipped iPhones. Earth Sci. Rev. 227, 103969,

841 https://doi.org/10.1016/j.earscirev.2022.103969

842 Thiele, S.T., Grose, L., Samsu, A., Micklethwaite, S., Vollgger, S.A., Cruden, A.R., 2017. Rapid,

843 semi-automatic fracture and contact mapping for point clouds, images and geophysical data. Solid

844 Earth, 8, 1241–1253, https://doi.org/10.5194/se-8-1241-2017

845 Visalli, R., Ortolano, G., Godard, G., Cirrincione, R., 2021. Micro-Fabric Analyzer (MFA): A New

846 Semiautomated ArcGIS-Based Edge Detector for Quantitative Microstructural Analysis of Rock Thin-

847 Sections. ISPRS Int. J. Geo-Inf.10, 51, https://doi.org/10.3390/ijgi10020051

848 Waters, D.J., 2001. The significance of prograde and retrograde quartz-bearing intergrowth

849 microstructures in partially melted granulite-facies rocks. Lithos 56, 97–110.

850 https://doi.org/10.1016/S0024-4937(00)00061-X

851 Westoby, M.J., Brasington, J., Glasser, N.F., Hambrey, M.J., Reynolds, J.M., 2012. 'Structure-from-

852 Motion'photogrammetry: A low-cost, effective tool for geoscience applications. Geomorphology 179,

853 300–314. https://doi.org/10.1016/j.geomorph.2012.08.021

854 White, R.W., Powell, R., Holland, T.J.B., Johnson, T.E., Green, E.C.R., 2014. New mineral activity–

855 composition relations for thermodynamic calculations in metapelitic systems. J. Metam. Geol. 32,

856 261–286, https://doi.org/10.1111/jmg.12071

857 Whitney, D.L., Evans, B.W., 2010. Abbreviation for names of rock-forming minerals. Am. Mineral.

858 95, 185–87, https://doi.org/10.2138/am.2010.3371

859 Yakymchuk C., 2020. Migmatites. In: Alderton D., Elias S.A. (Eds), Enciclopedia of Geology (Second

860 edition), Academic press, 492-501. https://doi.org/10.1016/B978-0-08-102908-4.00021-7

861 Zerboni, A., Perego, A., Cremaschi, M., 2015. Geomorphological map of the tadrart acacus massif

862 and the Erg Uan kasa (Libyan central sahara). J. Maps, 11(5), 772–778,

863 https://doi.org/10.1080/17445647.2014.955891

864 Zucali, M., Spalla, M.I., Gosso, G., 2002. Strain partitioning and fabric evolution As A correlation

865 tool: the example of the eclogitic micaschists complex in the SesiaLanzo Zone (Monte Mucrone e

866 Monte Mars, Western Alps Italy). Schweizerische Mineralogische und Petrographische Mitteilungen

867 82, 429–454.

868 Zucali, M., Manzotti, P., Diella, V., Pesenti, C., Risplendente, A., Darling, J., Engi, M. 2011. Permian

869 tectonometamorphic evolution of the Dent-Blanche Unit (Austroalpine domain, Western Italian

870 Alps). Rend. Online Soc. Geol. It. 15, 133–136.

871 Zucali, M., Corti, L., Delleani, F., Zanoni, D., Spalla, M.I., 2020. 3D reconstruction of fabric and

872 metamorphic domains in a slice of continental crust involved in the Alpine subduction system: The

873 example of Mt. Mucrone (Sesia–Lanzo Zone, Western Alps). Int. J. Earth Sci. 109(4), 1337–1354.

874 https://doi.org/10.1007/s00531-019-01807-6

875 Zucali M., Corti, L., Roda, M., Ortolano G., Visalli, R., Zanoni, D., 2021 Quantitative X-ray Maps

876 Analysis of Composition and Microstructure of Permian High-Temperature Relicts in Acidic Rocks

877 from the Sesia-Lanzo Zone Eclogitic Continental Crust, Western Alps. Minerals 11, 1421.

878 https://doi.org/10.3390/min11121421

879 Zucali, M., 2023. pyMinColab. Available at https://github.com/mzucali/pyMinColab/ (accessed 14
880 July 2023).

881 **Figure Captions**

882 **Fig. 1:** (a) Tectonic sketch map of the Alps showing the main units; (b) Geological map of the

883 Western Alps (modified after Roda et al., 2021). E: Etirol-Lèvaz; Em: Emilius; GR: Glacier Refray;

884 Pi: Pillonet; V: Vanoise; IIDK: II Zona Diorito-Kinzigitica.

885 **Fig. 2.** (a) Geological map of the DBTS (modified from Caso et al. 2024); (b) geological cross-section

886 (A – A') across the Arolla and Valpelline series.

887 **Fig. 3:** (a) view of the Lac Mort area during the drone flight; (b) 3D outcrop model acquired through

888 iPad 11" Pro equipped with LiDAR sensor; (c) point cloud of a 3D outcrop model processed in

889 CloudCompare for the structural data extraction; (d) yellow lines traced on the Google Satellite© in

890 Google Earth to be imported in QGIS for planes extraction.

891 **Fig. 4:** Micro-Fabric Analyzer workflow (modified after Visalli et al., 2021 and Caso, 2023).

892 **Fig. 5:** Summary of the main features of different cordierite-migmatitic gneiss samples collected in

893 different localities of the Valpelline Series.

894 **Fig. 6:** (a) S_1 foliation in a basic granulite level discordant respect to the external S_2 pervasive in

895 migmatite gneiss; (b) isoclinal F_2 affecting a brown amphibolite level; (c) isoclinal F_3 folds in

896 cordierite-migmatite gneiss; cordierite is folded and concentrated in fold hinges; (d) isoclinal F_3 folds

897 in cordierite-migmatite gneiss with local development of S_3 axial plane foliation made of sillimanite

898 and biotite, wrapping cordierite blasts; (e) asymmetric F_3 folds suggesting shearing of the short limb

899 and injection of melt along it (red arrows); (f) sheared brown amphibolite levels developing an "a-

900 type" flanking structure with leucosome as CE element; the sketch of the structure in the upper right

901 side is from Grasemann et al. (2003); (g) S_3 crenulation cleavage in migmatite gneiss; (h) two

902 pegmatitic dykes within migmatite (red arrows): the first is parallel to the S_2, the second cross-cut the

903 main and is gently folded; (i) two systems of pegmatitic dykes cross-cutting F_3 folds.

904 **Fig. 7:** (a) equal area stereographic projection (lower hemisphere; made with Stereonet 10;

905 Allmendinger et al., 2013; Cardozo and Allmendinger, 2013) of poles to S_1 foliation measured from

906 the field; (b) poles to S_1 foliations measured from LiDAR point clouds; (c) poles to S_2 foliations of

907 field data; (d) poles to S_2 foliations measured from LiDAR point cloud (blue dots with Kamb contour)

908 and from UAV point cloud (black dots); (e) A_2 fold axes (blue triangles) and axial planes (blue

909 planes); (f) projection of leucosomes discordant to the S_2 (planes measured on the field) and strikes

910 of leucosomes obtained from CloudCompare (rose diagrams); (g) poles to S_3 foliations, A_3 axes and

911 axial planes (measured on the field); (h) rose diagrams of the strikes of pegmatitic dykes measured

912 on the field; (i) pegmatite and aplites planes measured on the field; (j, k, l) dykes directions extracted

913 from LiDAR, UAV point clouds and Google Earth respectively.

914 **Fig. 8**: (a) thin section scan of the VP34 sample (XPL: crossed-polarized light); (b, c) thin section

915 scans of the 33SC sample (b is PPL: plane-polarized light; c: XPL).

Fig. 9: (a) S₂ foliation in the VP34 sample: the S₂ is marked by Sil II and Bt II (PPL); (b) quartz-feldspathic domain consists of elongated Qz II and Kfs in the VP34 sample (XPL); (c) S₂ microfold preserved within microlithon, whose limbs are paraller to S₃ foliation consisting of Sil III and Bt III in sample 33SC (PPL); (d) Grt porphyroblasts wrapped by the S₃ foliation (XPL); (e) S₃ made of Sil III and Bt III wrapping Crd blasts (XPL); (f) syn-kinematic (to S₃) flattened Grt porphyroblast wrapped by the S₃ foliation, showing an internal foliation in the rim concordant with the external S₃, made of sillimanite (XPL).

Fig. 10: Blastesis vs. deformation diagram of cordierite-migmatite gneiss.

Fig. 11: (a, b) mineral grain maps of the samples 33SC and VP34 respectively, obtained from the MFA toolbox; maps highlighting quarz-feldspathic domains in yellow are reported at the right and at the bottom respectively; (c) modal percentages of both samples obtained from the first cycle of Q-XRMA.

Fig. 12: (a) Long axis orientation rose diagrams for the main phases occurring in the two analysed samples; (b, c, d, e) long axis orientations maps of sillimanite, biotite, quartz and K-feldspar in sample VP34; f) long axis orientation map of sillimanite in sample 33SC (modified from Caso, 2023); (g) detail of figure f, showing a microdomains where the overprinting relationship between S₂ and S₃ are visible from long axis sillimanite orientation; in the bottom left the rose diagram shows data only of this zoom.
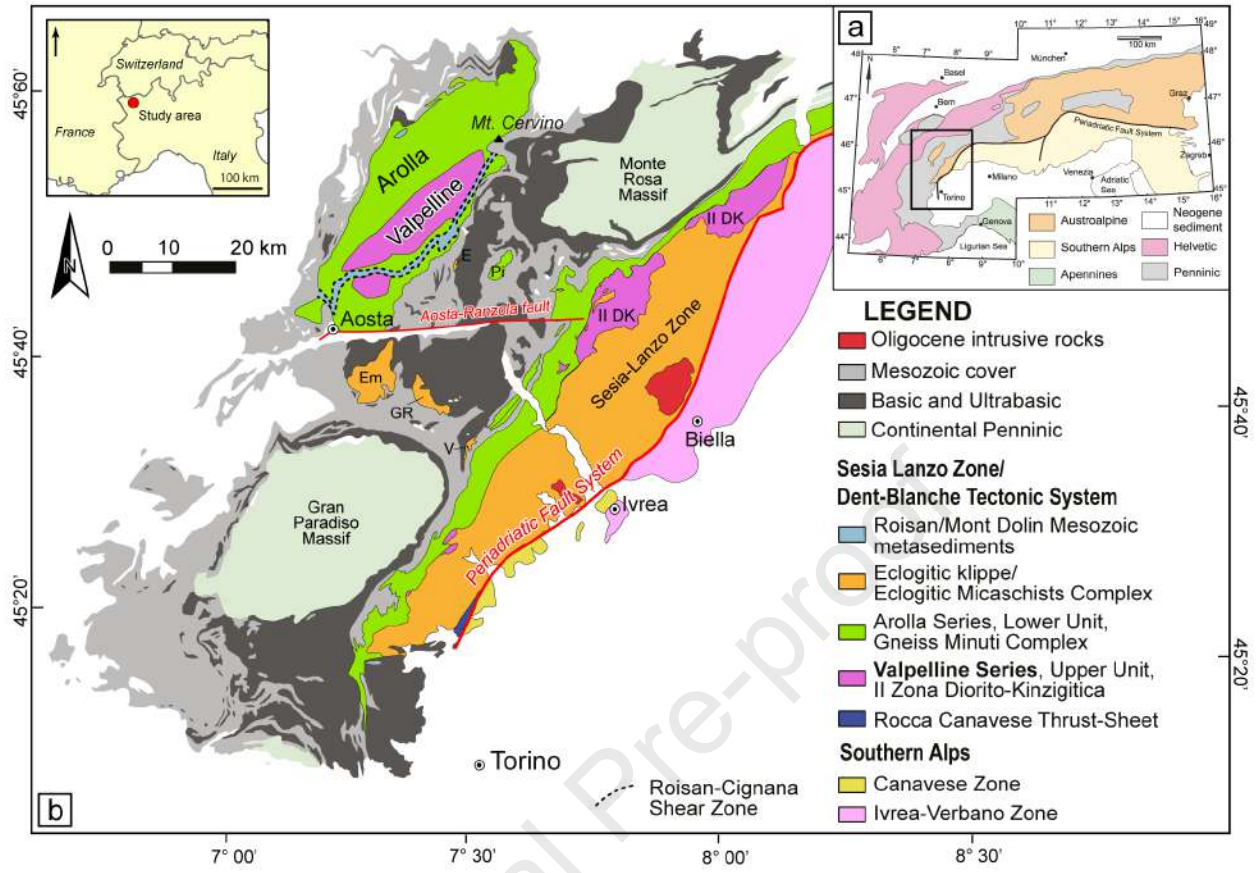
Fig. 13: (a) Roundness map of quartz and K-feldspar in sample VP34; (c) width/length ratio (roundness) of quartz grains in the sample VP34; (d) long axis orientation map of garnet grains in the sample 33SC; (e) roundness map of garnet in sample 33SC; (f) width/length ratio (roundness) of garnet grains in the sample 33SC.
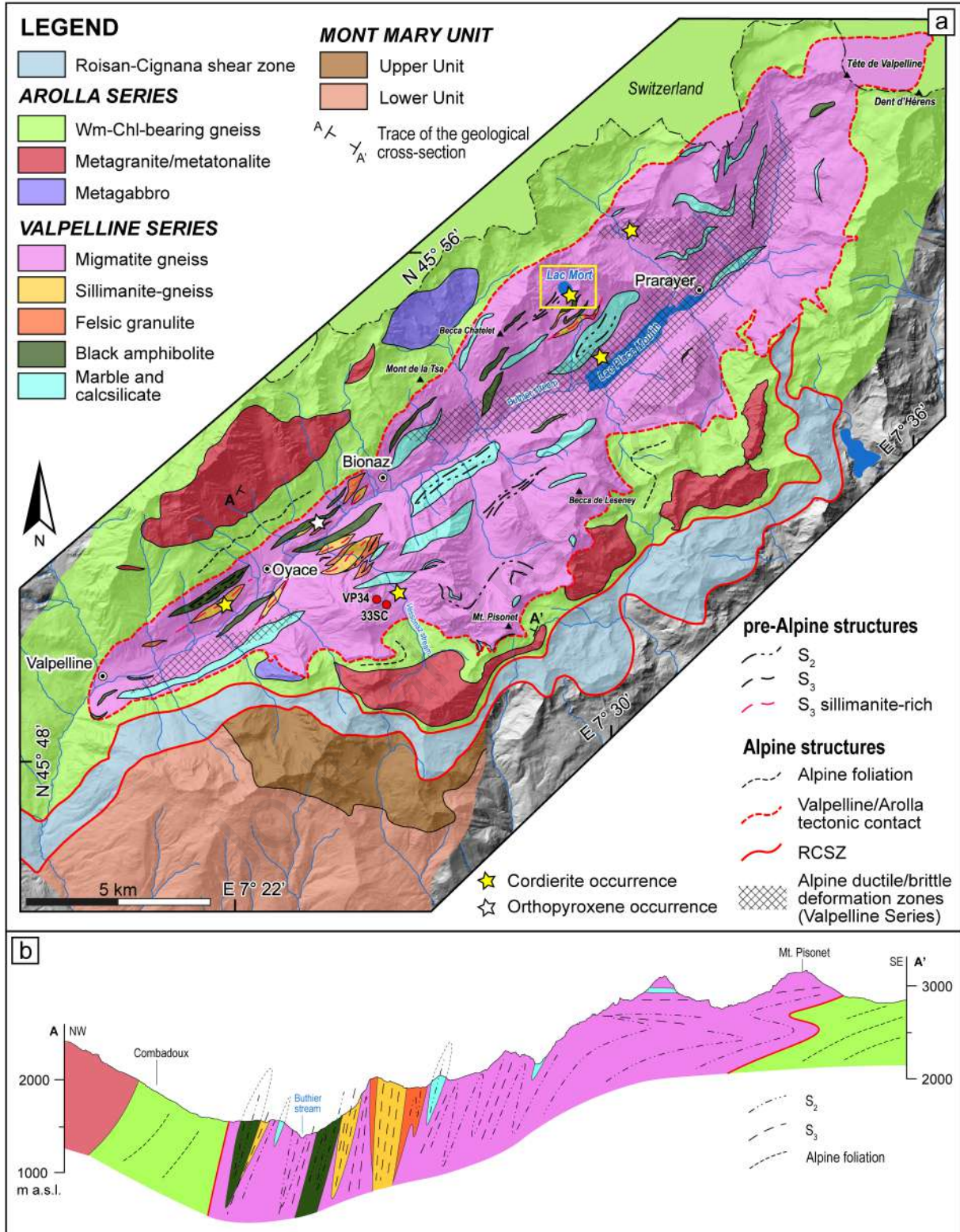
Fig. 14: (a) Mg apfu calibrated map of biotite; (b) Fe apfu calibrated map of biotite; (c) #Mg vs Ti apfu data of biotite extracted from each pixel of the calibrated map (black dots) and EMPA analyses
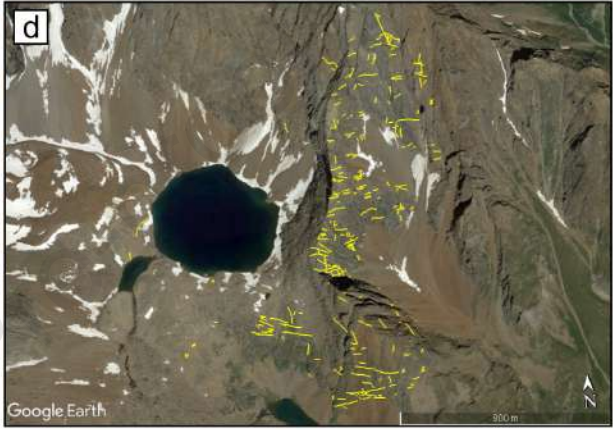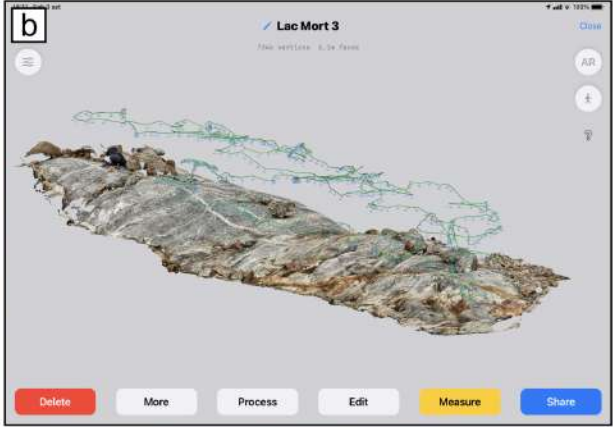
940   (discriminated on their microstructural positions) used for calibration with Q-XRMA (pink symbols);

941   (d) Ti apfu calibrated map of biotite; (e) Mg apfu calibrated map of garnet; (f) Fe apfu calibrated map

942   of garnet.

943   **Fig. 15:** Synoptic table summarizing the main features of the tectono-metamorphic stages defined in
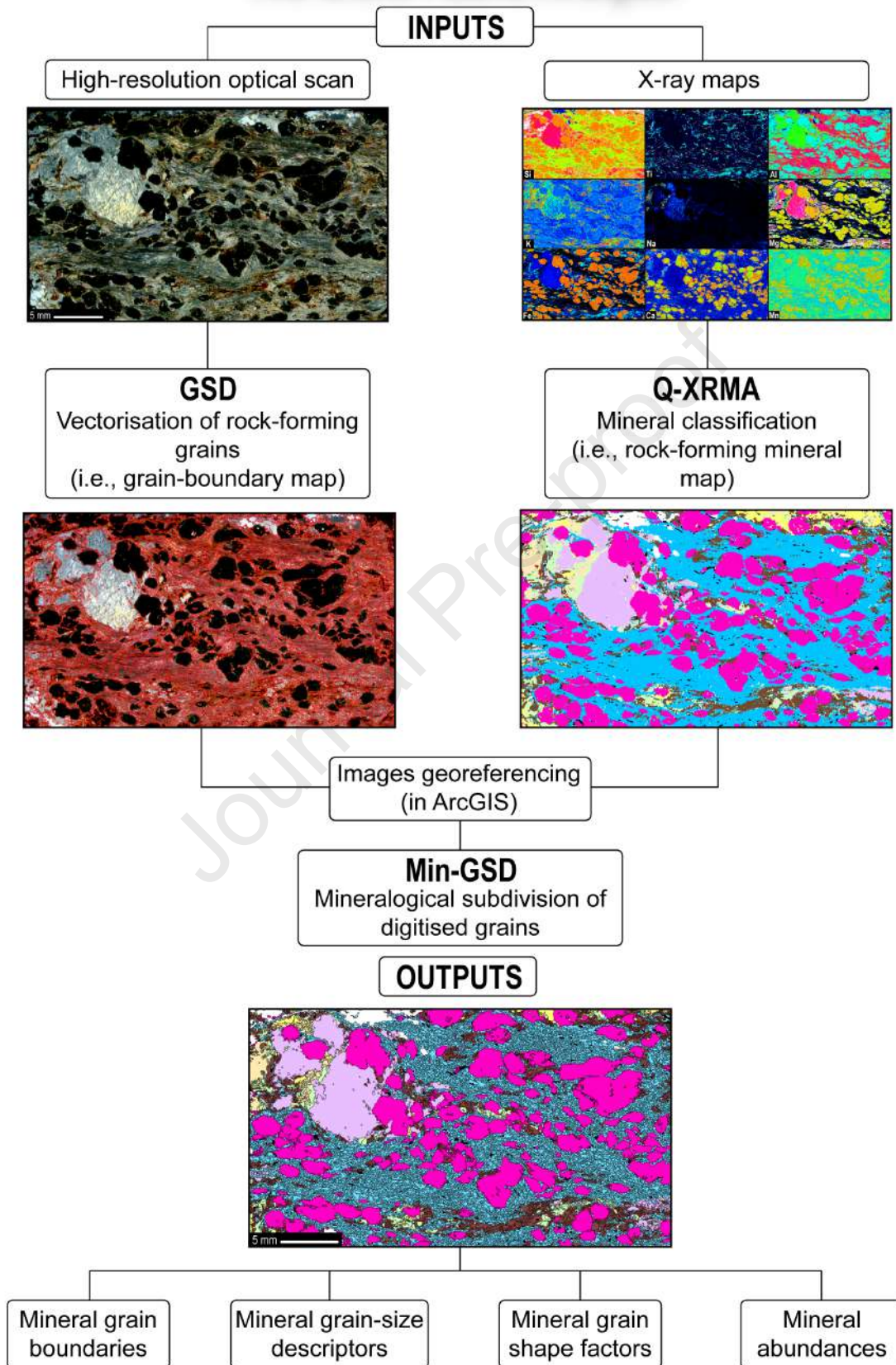
944   the Valpelline Series.

LEGEND

- Roisan-Cignana shear zone

AROLLA SERIES
- Wm-Chl-bearing gneiss
- Metagranite/metatonalite
- Metagabbro

VALPELLINE SERIES
- Migmatite gneiss
- Sillimanite-gneiss
- Felsic granulite
- Black amphibolite
- Marble and calcsilicate

MONT MARY UNIT
- Upper Unit
- Lower Unit

- Trace of the geological cross-section

pre-Alpine structures
- S_2
- S_3
- S_3 sillimanite-rich

Alpine structures
- Alpine foliation
- Valpelline/Arolla tectonic contact
- RCSZ
- Alpine ductile/brittle deformation zones (Valpelline Series)

- Cordierite occurrence
- Orthopyroxene occurrence

5 km

Switzerland

Tête de Valpelline
Dent d'Hérens

N 45° 56'

Lac Mort
Prarayer

Becca Chatelet
Mont de la Tsa

Bionaz

Becca de Leseney

Oyace

VP34
33SC

Mt. Pisonet

Valpelline

N 45° 48'

E 7° 36'
E 7° 30'
E 7° 22'

b

Mt. Pisonet
SE A'

3000

A NW

Combadoux

Buthier stream

2000

1000
m a.s.l.

2000

S_2
S_3
Alpine foliation

The Micro-Fabric Analyzer

INPUTS

High-resolution optical scan

X-ray maps

GSD
Vectorisation of rock-forming grains
(i.e., grain-boundary map)

Q-XRMA
Mineral classification
(i.e., rock-forming mineral map)

Images georeferencing
(in ArcGIS)

Min-GSD
Mineralogical subdivision of digitised grains

OUTPUTS

| Mineral grain boundaries | Mineral grain-size descriptors | Mineral grain shape factors | Mineral abundances |

Sample	Crd-locality	WGS coordinates	main features	
22CBP10	Grand Place, d'Orein stream	7.5035526 45.9372687	Foliation defined by Bt. Crd is strongly pinitised.	
6CP	N of Lac Mort	7.4827177 45.9213619	Foliation defined by Bt and locally minor fibrous Sil. Crd is strongly pinitised	
29SC	S of Lac Mort	7.4860345 45.9189366		
31SC	S of Lac Mort	7.48707993 45.91875192		
38SC	S of Lac Mort	7.48600577 45.91895677		
I_22_07	Lac Place Moulin	7.4991744 45.9032835	Foliation defined by Bt and minor Sil. Crd is strongly pinitised	
I_28_07	Lac Place Moulin	7.506861 45.907447		
22FC17A	Localitè La Ruine	7.364324 45.839654	Foliation defined by Bt and minor Sil. Crd is strongly pinitised	
VP34	Comba Vessonaz	7.4238788 45.8425377	Foliation defined by Sil and Bt. Crd idiomoprhic and always well preserved.	
VP44	Comba Vessonaz	7.4236035 45.8424476		
33SC	Comba Vessonaz	7.4268945 45.8418167		
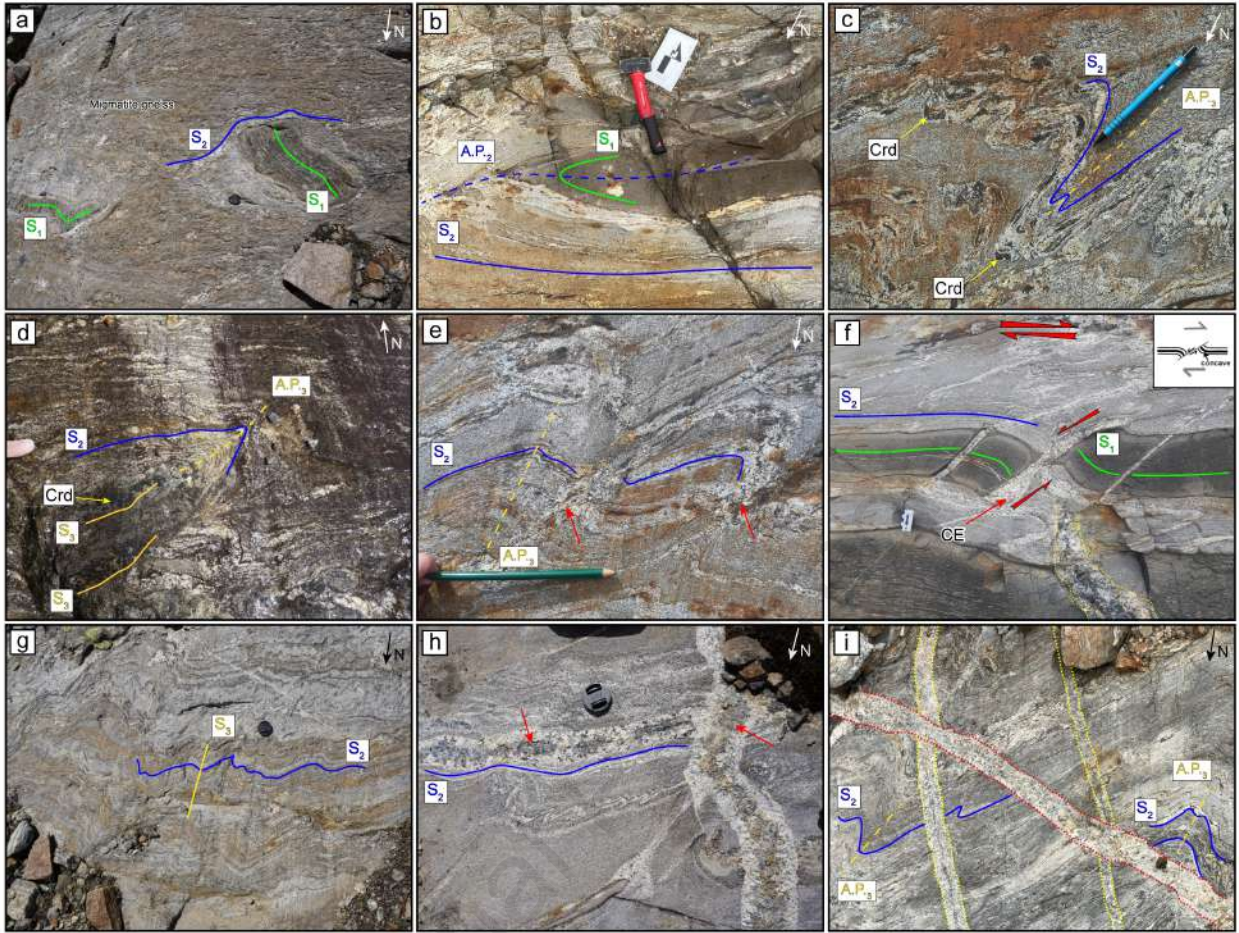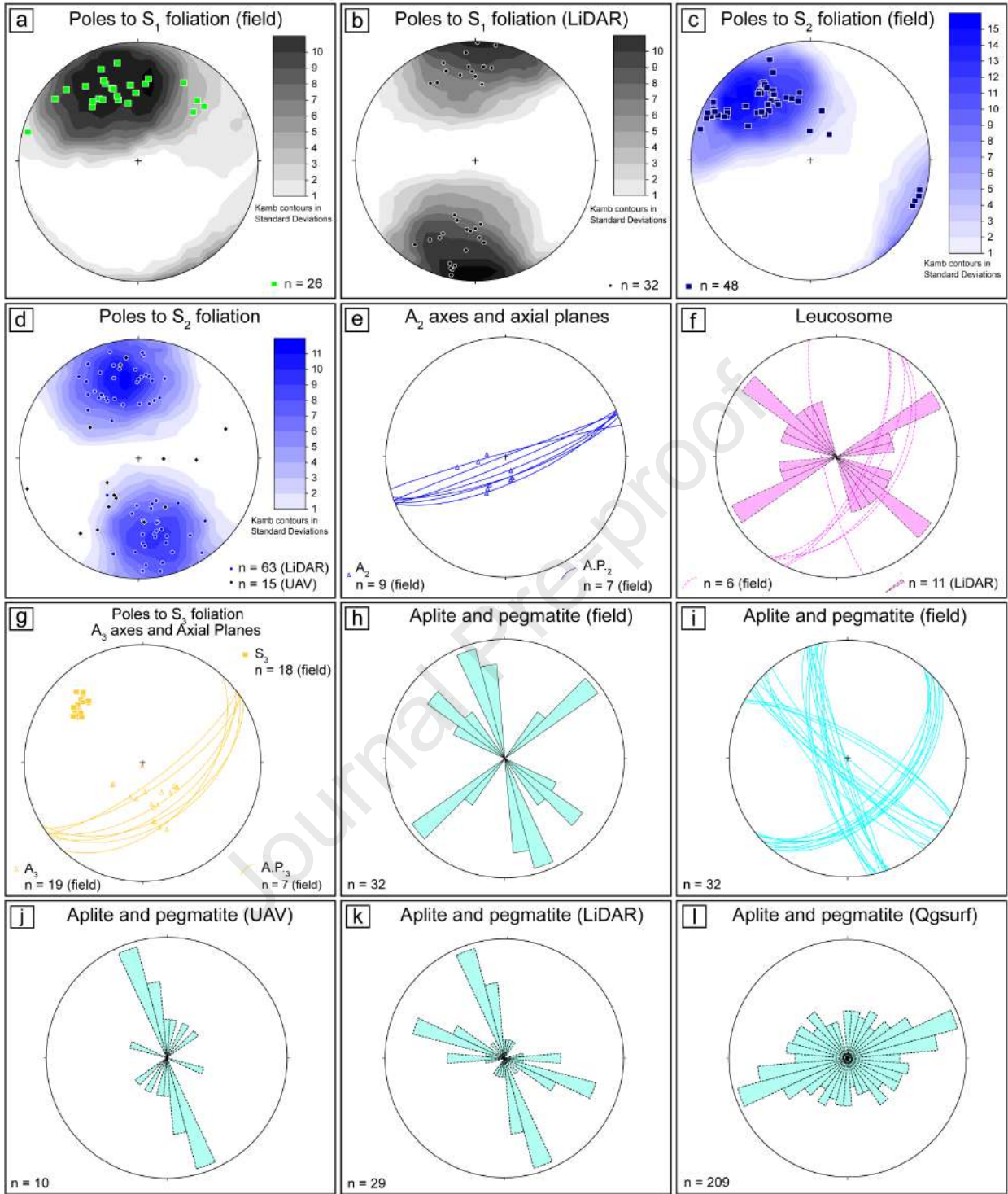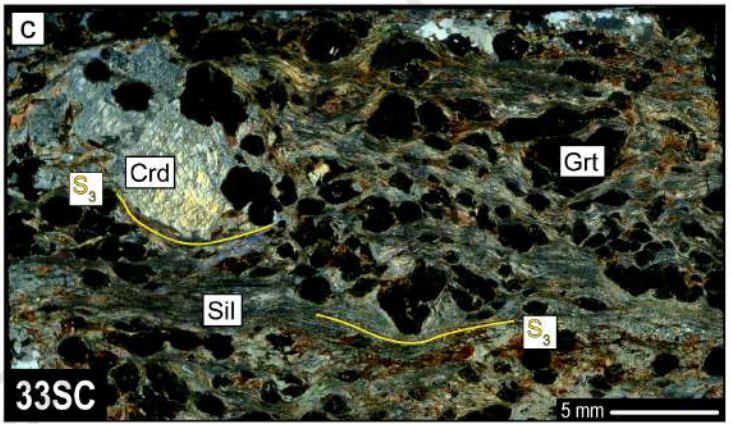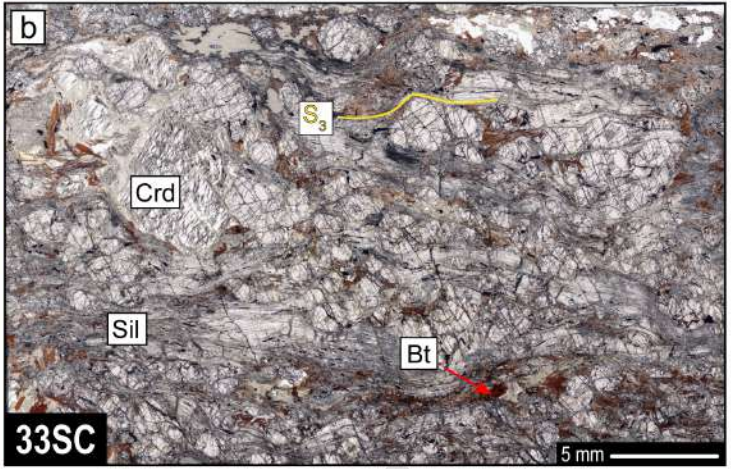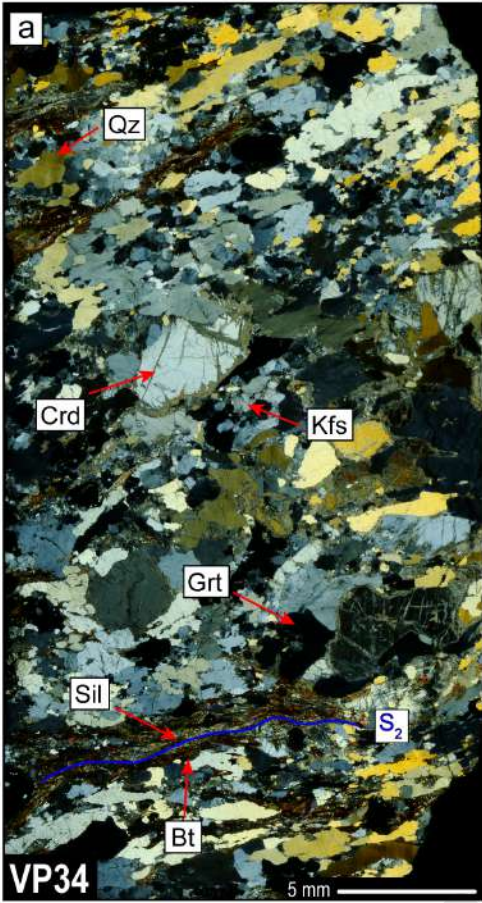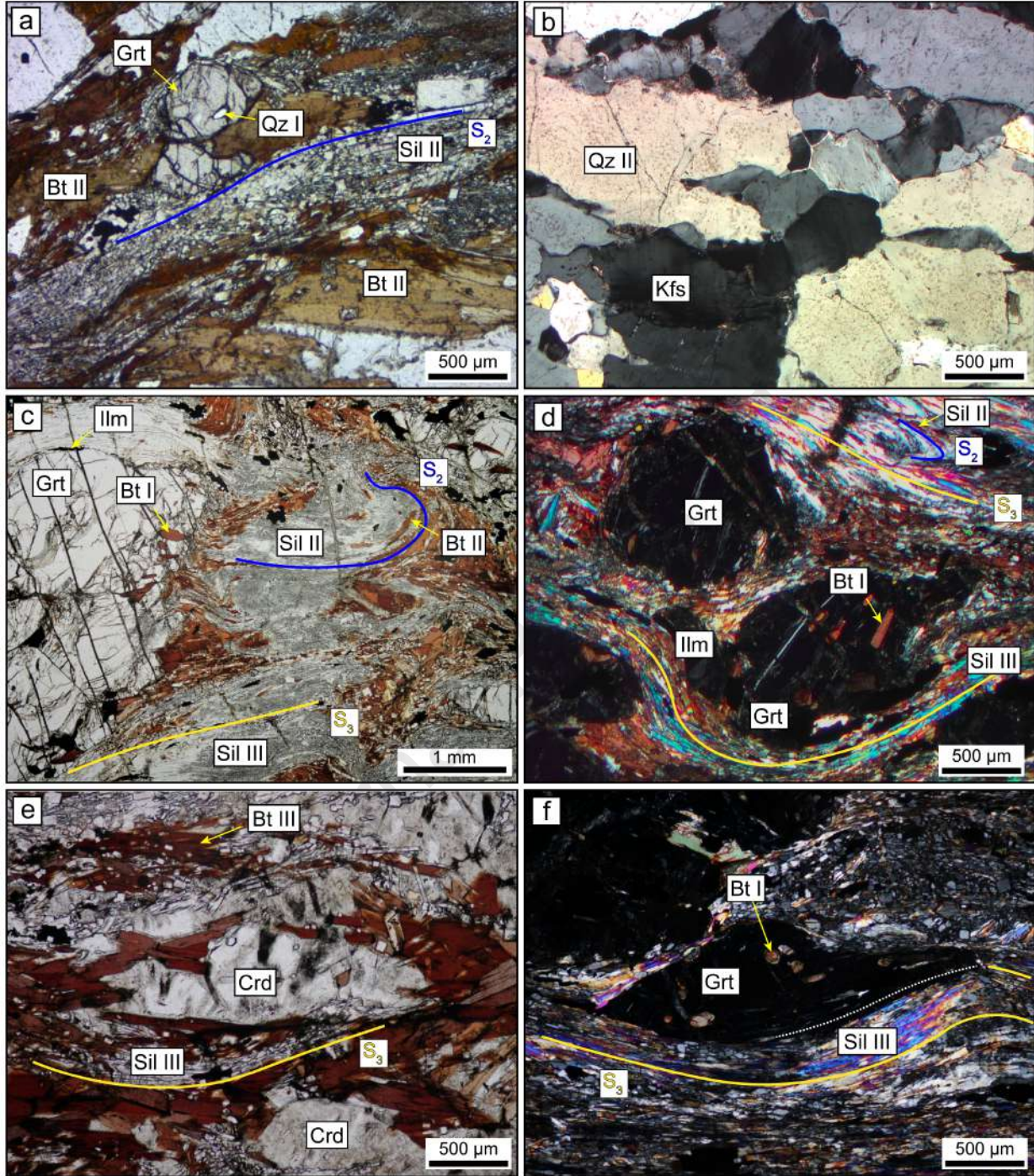
Stage	D$_1$ (?)	D$_2$	D$_3$
Fabric		S$_2$	S$_3$
Quartz	Qz I	Qz II	Qz III
Plagioclase			
K-feldspar			
Biotite	Bt I	Bt II	Bt III
Sillimanite	Sil I	Sil II	Sil III
Garnet		Grt II	
Cordierite			
Rutile	Rt I	Rt II	
Ilmenite			

D₁

S₁ foliation in basic granulite and brown amphibolite

Discordant to the S₂ foliation of migmatites

D₂

Isoclinal folding of the S₁ foliation and trasposition

Development of S₂ axial plane foliation

Melt production = leucosomes marking S₂.

early D₃

Isoclinal to asymmetric close folds with top-to-the W shearing

Local development of S₃ axial plane foliation

Cordierite makes deformed aggregates in fold hinges

Pegmatitic dykes start intrude migmatites and are locally folded.

late D₃

Different systems of pegmatitic dykes cross-cutting each other and all the migmatitic structures

Three systems:
1) parallel to the S₂ foliation, affected by boudinage
2) striking NNW-SSE, locally folded;
3) striking NW-SE, cross-cutting all the previous ones

Metabasite: Opx + Cpx + Pl

Migmatite: Bt I + Sil I + Qz I

Bt II + Sil II + **Grt + Crd + melt**

Bt III + Sil III + Ilm ± Grt

Basic granulite   Brown amphibolite   Leucosomes   Pegmatitic dykes   Grt   folded Crd   Crd

Highlights:

- Combination of traditional field-based and remote-sensing derived structural analysis
- Extraction of structural data from LiDAR and UAV-derived 3D outcrop models
- Quantitative microstructural analysis and shape parameters extraction from vectorised grains
- Combination of quantitative meso- and microstructural analysis with mineral-chemical data
- Multiscale structural analysis applied to the Valpelline Series (Dent-Blanche Nappe)

Declaration of competing interest

The authors declare that they have no competing financial interests or personal relationships that could have appeared to influence the work reported in this paper.